

# Scale and spatial distribution assessment of rainfall-induced landslides in a catchment with mountain roads

Chih-Ming Tseng<sup>1</sup>, Yie-Ruey Chen<sup>1</sup>, Szu-Mi Wu<sup>2</sup>

5 <sup>1</sup>Department of Land Management and Development, Chang Jung Christian University, Tainan, 71101, Taiwan.  
<sup>2</sup>Chen-Du Construction Limited, Taoyuan, 33059, Taiwan.

*Correspondence to:* Chih-Ming Tseng (cmtseng@mail.cjcu.edu.tw)

**Abstract.** This study focused on landslides in a catchment with mountain roads that were caused by Nanmadol (2011) and Kong-rey (2013) typhoons. Image interpretation techniques were employed to interpret satellite images captured before and after the typhoons to derive the surface changes changes in slope surfaces. A The multivariate hazard evaluation method was adopted to establish a landslide susceptibility assessment model. The evaluation of landslide locations and relationship between landslide and predisposing factors is preparatory for assessing and mapping landslide susceptibility. We then mapped landslide susceptibility and locations to determine the relationship between the spatial distribution of landslide areas and the natural environment along mountain roads. The results can serve as a reference for preventing and mitigating slope disasters on mountain roads.

10  
15

## 1 Introduction

Taiwan is an island of which three quarters of its land area consists of slope land that is 100 m above sea level, or is less than that but has an average gradient of 5% above (Soil and Water Conservation Bureau, 2012). Much of this sloped land has a steep gradient and fragile geological formations. Taiwan is hit by an average of 3.4 typhoons every year during years 1911 to 2016 (Central Weather Bureau, 2017). In additions, an average annual rainfall reach 2,506 mm in years 1949 to 2012 (Water Resources Agency, 2017). Typhoons usually occur between July and October, and 70%–90% of the annual rainfall is composed of heavy rain directly related to typhoons (SWCB, 2012). Concentrated rainfall causes heavy landslides and debris flows every year (Dadson et al., 2004). The threat of disaster currently influences industrial and economic development and the road networks in endangers areas; thus, establishing disaster evaluation mechanisms is imperative.

20  
25

Landslide susceptibility can be evaluated by analysing the relationships between landslides and various factors that are responsible for the occurrence of landslides (Brabb 1984; Guzzetti et al., 1999a, Guzzetti et al., 2005). In general, the factors affect landslides including predisposing factors (e.g., geology, topography, and hydrology) and triggering factors (e.g., rainfall, earthquakes, and anthropogenic factors) (Chen et al., 2013a; Chen et al., 2013b; Chue et al., 2015). Geological factors include lithological factors, structural conditions, and soil thickness; topographical factors include slope, aspect, and

elevation; and anthropogenic factors include deforestation, road construction, land development, mining, and alterations of surface vegetation (Chen et al., 2013a; Chen et al., 2013b; Chue et al., 2015). The method used to assess landslide susceptibility can be divided into qualitative and quantitative. Qualitative methods are based completely on field observations and an expert's priori knowledge of study area (Stevenson, 1977; Anbalagan, 1992; Gupta and Anbalagan, 1997). Some qualitative approaches incorporate ranking and weighting, and become semi-quantitative (Ayalew and Yamagishi, 2005). For examples the Analytic Hierarchy Process (AHP) (Saaty, 1980; Barredo et al., 2000; Yoshimatsu and Abe, 2006; Kamp et al., 2008; Yalcin, 2008; Kayastha et al., 2013; Zhang et al., 2016) and the weighted linear combination (WLC) (Jiang and Eastman, 2000; Ayalew et al., 2005; Akgün et al., 2008). Quantitative methods apply mathematical models to assess the probability of landslide occurrence, and thus define hazard zones on a continuous scale (Guzzetti et al., 1999b). Quantitative methods developed to detect the areas prone to landslide can be divided mainly into two categories: deterministic approach and statistical approach. The deterministic approach is based on the physical laws driving landslides (Okimura and Kawatani, 1987; Hammond et al., 1992; Montgomery and Dietrich, 1994; Wu and Sidle, 1995; Gökceoglu and Aksoy, 1996; Pack et al., 1999; Iverson, 2000; Guimarães et al., 2003; Xie et al., 2004) and are generally more applicable when the underground conditions are relatively homogeneous and the landslides are mainly slope dominated. The statistical approach is based on the relationships between the affecting factors and past and present landslide distribution (Van Westen et al., 2008). Statistical methods analyze the relation between predisposing factors affecting the landslide which include bivariate statistical models (Van Westen et al., 2003; Süzen and Doyuran, 2004; Thiery et al., 2007; Bai et al., 2009; Constantin et al., 2011; Yilmaz et al., 2012), multivariate statistical approaches as discriminant analysis (Baeza and Corominas, 2001; Carrara et al., 2003; Carrara et al., 2008; Pellicani et al., 2014), and linear and logistic regression (Dai and Lee, 2002; Ohlmacher and Davis, 2003; Ayalew and Yamagishi, 2005; Yesilnacar and Topal, 2005; Greco et al., 2007; Carrara et al., 2008; Lee et al., 2008; Pellicani et al., 2014), as well as nonlinear methods such as artificial neural networks (ANN) (Lee et al., 2004; Yesilnacar and Topal, 2005; Kanungo et al., 2006; Wang and Sassa, 2006; Li et al., 2012), multivariate hazard evaluation method (MHEM) (Su et al., 1998; Lin et al., 2009). The MHEM is a nonlinear mathematical model that presents an instability index to indicate landslide susceptibility (Lin et al., 2009). In additions, some studies, landslide susceptibility analyses have focused on man-made facilities such as roads and railroads and have examined the landslide susceptibility of surrounding environments (Das et al., 2010; Pantelidis, 2011; Das et al., 2012; Devkota et al., 2013; Martinović et al., 2016; Pellicani et al., 2016; Pellicani et al., 2017). The aforementioned studies on the landslide susceptibility of areas surrounding man-made facilities have not investigated characteristics such as the location and scale (area) of landslides occurring in upper or lower slopes, and such characteristics thus constituted one of the objectives of the present study.

Technological progress has provided various advanced tools and techniques for land use monitoring. In recent years, aerial photos or satellite images have been commonly used in post disaster interpretations and assessments of landslide damage on large-area slopes (Erbek et al., 2004; Lillesand et al., 2004; Nikolakopoulos et al., 2005; Lin et al., 2005; Chen et al., 2009; Otukey and Blaschke, 2010; Chen et al., 2013a). Satellite images offer the advantages of short data acquisition cycles, swift

understanding of surface changes, large data ranges, and being low cost, particularly for mountainous and inaccessible areas. With the assistance of computer analysis and geographic information system (GIS) platforms, researchers can quickly determine land cover conditions. Thus, satellite images are suitable for investigating large areas and monitoring temporal changes in land use (Liu et al., 2001). Satellites can capture images of the same area multiple times within a short period; the images are consistent in quality and are digitized, rendering them convenient for computer applications. Studies have indicated that land surface change detection is the process of exploring the differences between images captured at different times. With multispectral satellite images, land surface interpretations involve comparisons of multitemporal images that are completely geometrically aligned (Liu et al., 2001; Chadwick et al., 2005; Chen et al., 2009; Chue et al., 2015).

We selected part of Provincial Highway No. 20 in the catchment area of Laonung River in southern Taiwan as our study area.

Regarding time, we focused on periods before and after landslides that occurred in the study area as a result of Typhoon Nanmadol (2011) and Typhoon Kong-rey (2013). We applied the maximum likelihood method to interpret and categorize high-resolution satellite images, thereby determining the land surface changes and landslides in the study area before and after the rainfall events. By using a GIS platform, we constructed a database of the rainfall and natural environment factors.

Subsequently, we developed a landslide susceptibility assessment model by using the MHEM, the model performance then was verified by historical landslides. In additions, we extracted the locations of landslide areas to explore the relationship between the natural environment and the spatial distribution of the scale of these areas. The results of this study could serve as a reference for the prevention and mitigation of slope disasters on hillsides in a catchment with mountain roads.

## 2 Methodology

### 2.1 Maximum likelihood

The maximum likelihood classifier is a supervised classification method (SCM). SCMs include three processing stages: training data sampling, classification, and output. The underlying principle of supervised classification is the use of spectral pattern recognition and actual ground surface data to determine the types of data required and subsequently select a training site, which has a unique set of spectral patterns. To accurately estimate the various spectral conditions, the spectral patterns of the same type of feature are combined into a coincident spectral plot before the class of the training site is selected. Once training has been completed, the entire image is classified based on the spectral distribution characteristics of the training site by using statistical theory for automatic interpretation (Lillesand et al., 2004).

To facilitate the calculation of probability in the classification of unknown pixels, the maximum likelihood method assumes a normal distribution in the various classes of data. Under this assumption, the data distribution can be expressed using covariance matrices and mean vectors, both of which are used to calculate the probability of a pixel being assigned to a land cover class. In other words, the probability of  $X$  appearing in class  $i$  is calculated using Eq. (1), and the highest probability is used to determine the feature of each pixel (Lillesand et al., 2004).

$$p(X|C_i) = (2\pi)^{d/2} |\Sigma_i|^{-1/2} \exp\left[-\frac{1}{2}(X - \mu_i)^T \Sigma_i^{-1} (X - \mu_i)\right] \quad (1)$$

$$x = \begin{bmatrix} x_1 \\ x_2 \\ \vdots \\ x_d \end{bmatrix} \quad \mu_i = \begin{bmatrix} \mu_{1i} \\ \mu_{2i} \\ \vdots \\ \mu_{di} \end{bmatrix} \quad \Sigma_i = \begin{bmatrix} S_{11} & S_{12} & \cdots & S_{1d} \\ S_{21} & S_{22} & \cdots & S_{2d} \\ \vdots & \vdots & \ddots & \vdots \\ S_{d1} & S_{d2} & \cdots & S_{dd} \end{bmatrix}$$

In this equation,

$d$  denotes the number of features;

5  $X$  denotes a sample expressed using features and has  $d$  dimensions;

$p(X|C_i)$  denotes the probability that  $X$  originates from class  $i$ ;

$\Sigma_i$  denotes the covariance matrix of class  $i$ ;

$\Sigma_i^{-1}$  denotes the inverse matrix of  $\Sigma_i$ ;

$|\Sigma_i|$  denotes the determinant of  $\Sigma_i$ ;

10  $\mu_i$  denotes the mean vector of classification  $i$ ;

$(x - \mu_i)^T$  denotes the transpose matrix of  $(x - \mu_i)$ ; and

$S_{ij}$  denotes the covariance of classes  $i$  and  $j$ .

During classification, the maximum value of the probability density functions of sample  $X$  in each class is used to determine which class the sample belongs to. The maximum likelihood classification decision is shown in Eq. (2).

15

$$X \in C_m, \quad m \in \{1, 2, \dots, k\}$$

if

$$p(X|C_m) = \max\{p(X|C_j), \quad j = 1, 2, \dots, k\} \quad (2)$$

The question in classification is how to effectively separate the classes in the feature space, or in other words, how to divide the feature space. Maximum likelihood is a common approach that offers fairly good classification accuracy (Bruzzone and Prieto, 2001; Chen et al., 2004). Thus, we adopted maximum likelihood to interpret and classify the satellite images.

## 2.2 Accuracy assessment

This study employed the aforementioned maximum likelihood method to classify satellite images. To determine whether the accuracy of image classification was acceptable, we adopted an error matrix to test for accuracy. An error matrix is a square matrix that presents error conditions in the relationship between ground surface classification results and reference data (Verbyla, 1995). Such a matrix contains an equal number of columns and rows, and the number is determined by the number of classes. For example, Table 1 contains four classes. The columns show the reference data, and the rows show the

classification results. The various elements in the table indicate the quantity of data corresponding to each combination of classes.

In the table,  $X_{12}$  represents the amount of data that was interpreted as Class A but actually belongs to Class B, whereas  $X_{21}$  indicates the amount of data that was interpreted as Class B but actually belongs to Class A.  $X_{11}$  and  $X_{22}$  represent the amount of data accurately classified as Class A and Class B, respectively. An error matrix is generally used to check the quality of classification results in statistics (Congalton, 1991; Verbyla, 1995). In the present study, we evaluated the accuracy of the classification results based on the overall accuracy ( $OA$ ) and  $Kappa$  value (Cohen, 1960), which is the coefficient of agreement derived from the relationship between the classification results and training data. These two parameters are explained as follows.

### 10 2.2.1 $OA$

$OA$  is the simplest method of overall description. For all classes,  $OA$  represents the probability that any given point in the area will be classified correctly.

$$OA = \left[ \frac{1}{N} \sum_{i=1}^n X_{ii} \right] \times 100\% \quad (3)$$

In Eq. (3),  $N$  denotes the total number of check points and  $X_{ii}$  denotes the number of correctly classified checkpoints.

### 15 2.2.2 $Kappa$ coefficient

The  $Kappa$  ( $\hat{K}$ ) coefficient indicates the degree of agreement between the classification results and reference values and shows the percentage reduction in the errors of a classification process compared with the errors of a completely random classification process. Generally, the  $Kappa$  coefficient ranges from 0 to 1, and a greater value indicates a higher degree of agreement between the two sets of results, as shown in Eq. (4):

$$20 \quad \hat{K} = \frac{N \sum_{i=1}^n X_{ii} - \sum_{i=1}^n (X_{i+} \times X_{+i})}{N^2 - \sum_{i=1}^n (X_{i+} \times X_{+i})} \times 100\% \quad (4)$$

As reported by Landis and Koch (1977), a  $Kappa$  coefficient greater than 0.8 signifies a high degree of accuracy, whereas a coefficient between 0.4 and 0.8 or less than 0.4 indicates moderate or poor accuracy, respectively.

## 2.3 Rainfall analysis method

In previous studies regarding the influence of rainfall on landslides, rainfall intensity and accumulated rainfall have been most commonly used as predisposing causal factors of landslides (Giannecchini, 2006; Chang et al., 2007; Giannecchini et al., 2012; Ali et al., 2014). Therefore, we adopted effective accumulated rainfall ( $EAR$ ) and intensity of rolling rainfall ( $I_R$ ) as rainfall indices and predisposing impact factors of landslides in the present study. These two indices are explained as follows.

### 2.3.1 EAR

Generally, rainfall is considered the trigger of slope collapse, whereas previous rainfall can be regarded as a potential factor of a landslide. Previous rainfall influences the water content of the soil, which in turn affects the amount of rainfall required to trigger a landslide (Seo and Funasaki, 1973).

- 5 Figure 1 shows an illustration of rainfall events defined based on *EAR* (Seo and Funasaki, 1973). The diagram shows a concentrated rainfall event with no rainfall in the preceding or subsequent 24 hours and can thus be considered a continuous rainfall event. A continuous rainfall event that occurs simultaneously with a landslide is the main rainfall event. The beginning of the main rainfall event is defined as the time point when the rainfall first reaches 4 mm. The calculation of accumulated rainfall ends at the time when the landslide occurs. However, because the exact time of a landslide cannot be  
10 precisely determined, we regarded the hour with the maximum rainfall during the main rainfall event as the time when the landslide occurred in this study.

In accordance with previous studies, we defined *EAR* as the sum of direct and previous indirect rainfall. Previous indirect rainfall is the rainfall accumulated during the 7 days prior to the main rainfall event and can be expressed as follows (Seo and Funasaki, 1973; Crozier and Eyles, 1980):

$$15 \quad \sum_{n=1}^7 k^n P_n = P_b \quad (5)$$

where  $P_b$  denotes the previous indirect rainfall,  $P_n$  denotes the rainfall during the  $n$  days prior to the main rainfall event (mm), and  $k$  denotes a diminishing coefficient set as 0.9 in this study (Chen et al., 2005). Direct rainfall encompasses the continuous rainfall accumulated during the rainfall events, starting from the first rainfall to the time of landslide occurrence. Direct rainfall has a direct and effective impact on landslide occurrence and is thus not diminished. Therefore, *EAR* could be

- 20 expressed as follows in this study:

$$EAR = P_r + P_b \quad (6)$$

where  $P_r$  (mm) represents the rainfall accumulated during the main rainfall event from the first rainfall to the time of landslide occurrence, and  $P_b$  (mm) represents the previous indirect rainfall.

### 2.3.2 $I_R$

- 25 Rainfall intensity refers to the amount of rainfall within a unit of time. It is considered a crucial index for evaluating disasters because greater intensity or longer durations have considerable impacts on slope stability. Furthermore, rainfall-induced landslides may be triggered by several hours of continuous rainfall. The raw rainfall data in this study was hourly precipitation; thus,  $I_R$  (mm/h) can be expressed as follows:

$$I_{mR} = \sum_{t-m+1}^m I = I_{t-m+1} + I_{t-m+2} + \dots + I_t \quad (7)$$

where  $I$  denotes rainfall intensity,  $m$  denotes the number of rolling hours of rainfall (set as 3 hours in this study),  $I_{mR}$  denotes the  $I_R$  during  $m$  hours, and  $I_t$  denotes the rainfall intensity during hour  $t$ .

## 2.4 MHEM

- 5 The MHEM is a diverse non-linear mathematical model. Based on relative relationships, the MHEM presents an instability index ( $D_i$ ) to indicate susceptibility risk in different areas. The objective is to analyze the variability of landslide-inducing factors and estimate the variance of causal predisposing factors and then to determine the weight of each factor according to the value of variance, finally to derive a suitable landslide susceptibility assessment model (Su, et al., 1998; Lin et al., 2009; Chue, et al., 2015).
- 10 The causal predisposing factors in the MHEM are rated based on the frequency of landslide occurrence, which is calculated as follows:

$$R_i = \frac{r_i}{r_T} \quad (8)$$

where  $R_i$  represents the landslide pixel grid ratio of the various factors in class grade  $i$ ,  $r_i$  represents the number of landslide pixels grids in class grade  $i$ , and  $r_T$  represents the total number of pixels grids. Thus, landslide percentage  $X_i$  is expressed as

$$15 \quad X_i = \frac{R_i}{\sum R_i} \quad (9)$$

where  $X_i$  denotes the landslide percentage of class grade  $i$  and  $\sum R_i$  denotes the sum of the landslide pixel grid ratios.

Based on the landslide percentages of the various classes for each predisposing causal factor, the normalized score value of classes for each factor can be calculated using Eq. (10), and presented in relative values ranging from 1 to 10.

$$d_n = \frac{9(X_i - X_{\min})}{(X_{\max} - X_{\min})} + 1 \quad (10)$$

- 20 In Eq. (10),  $X_i$  represents the causal rate of the sample region and  $X_{\max}$  and  $X_{\min}$  represent the maximum and minimum landslide percentages of the factor in the various sample regions, respectively.

To estimate the weight of influence of each predisposing causal factor, the coefficient of variation ( $V$ ) of the landslide ratios derived from the class grade of the predisposing impact factors is used to represent the sensitivity of landslide ratios in different predisposing impact factor classes grades. A smaller coefficient of variation denotes higher similarity among the

- 25 landslide probabilities in the various classes grades, which indicates that this factor grading method cannot determine which areas have higher or lower landslide probabilities. By contrast, a greater coefficient of variation denotes that this factor grading method can be used to describe the influence of factor classes grades on landslides. Thus, the coefficient of variation

among the predisposing impact factors can indicate the factor weights. The coefficient of variation is calculated as shown in Eq. (11):

$$V = \frac{\sigma}{X} \times 100\% \quad (11)$$

where  $\sigma$  is the standard deviation and  $X$  is the mean landslide percentage of the various factor classes grades.

- 5 We divided the coefficient of variation of each individual factor by the total coefficient of variation of all factors to derive the factor weight, which represented the degree of influence of the factor on landslide occurrence. The factor weight can be calculated as shown in Eq. (12), where  $W$  is the factor weight and  $V$  is a coefficient of variation.

$$W_i = \frac{V_i}{V_1 + V_2 + \dots + V_n} \quad (12)$$

- 10 Finally, the weight ( $W_i$ ) of each factor is determined by the rank of its variance ( $V$ ), and each factor is assigned a different weight. Subsequently, a nonlinear mathematical model can be derived as follows:

$$D_t = d_1^{W_1} \times d_2^{W_2} \times d_3^{W_3} \times d_4^{W_4} \times d_5^{W_5} \dots \times d_n^{W_n} \quad (13)$$

where  $D_t$  is the instability index of the samples, expressed using relative values ranging from 1 to 10. A cumulative value closer to 10 indicates greater landslide potential, whereas a cumulative value closer to 1 indicates lower landslide potential.

- 15 By using the concept of log-normal distribution in statistics, we converted the levels of instability index derived using the MHEM into probabilities of landslide occurrence. The calculation formula of the log-normal distribution is shown in Eq. (14):

$$P(F) = \frac{1}{x\sigma\sqrt{2\pi}} e^{-\frac{1}{2}[(\ln x - \mu)/\sigma]^2} \quad (14)$$

- 20 where  $x$  denotes the level of the instability index and  $\mu$  and  $\sigma$  denote the mean and standard deviation of the level of the instability index, respectively. After calculating the probabilities of landslide occurrence by using the log-normal distribution, we normalized the probabilities to range from 0 to 1 for convenience. The normalization formula is shown in Eq. (15).

$$P(F)' = \frac{(X_i - X_{\min})}{(X_{\max} - X_{\min})} \quad (15)$$

In Eq. (15),  $X_i$  represents the factor being normalized and  $X_{\max}$  and  $X_{\min}$  represent the maximum and minimum values of the factor, respectively.



### 3 Study area

We referred to the historical data on road disasters from the NCDR (2017) and considered road sections where rainfall-induced landslides occurred frequently in southern Taiwan. We focused on the periods before and after Typhoon Nanmadol (2011) and Typhoon Kong-rey (2013) hit southern Taiwan, and we selected part of Provincial Highway No. 20 in the catchment area of Laonung River in southern Taiwan as our study area (Fig. 2), which includes areas from three districts in Kaohsiung City (Jiasian, Liouguei, and Taoyuan). The Laonung River flows SW cross over the southern of study area which originating from the Jade Mountain. The study area is located in a tropical monsoon climate zone. According to the climate statistics (1983 - 2012) recorded from the Central Weather Bureau, the average annual rainfall is approximate 2,758 mm.

### 4 Image interpretation and classification

#### 10 4.1 Preprocessing of satellite images

This study employed and interpreted satellite images taken by FORMOSAT-2 (FM2). FM2 images have been extensively used to identify natural disasters and land use (e.g., Lin et al., 2004; Lin et al., 2006; Liu et al., 2007; Chen et al., 2009, Lin et al., 2011; Chen et al., 2013a). In the present study, prior to interpretation, the satellite images underwent spectral fusion, coordinate positioning, cropping, and cloud removal. The images taken by FM2 are multispectral with blue, green, red, and near-infrared (NIR) wavelengths (Chen et al., 2013a; Chue et al., 2015). Image fusion and coordinate positioning were conducted using the import data and coordinate positioning tool of ERDAS IMAGINE (2013). Because clouds and shadows affect the accuracy of image interpretations, we used the image analysis tool of ArcGIS to remove clouds from the images.

#### 4.2 Training site selection and mapping

To map the sample areas required for image interpretation, we overlapped the high-resolution, preprocessed satellite images of the study area before and after the typhoons and mapped the training sites by using a GIS platform. Based on field investigations and relevant studies (Chen et al., 2009; Chen et al., 2013a; Chue et al., 2015), we selected areas with water, roads, buildings, crops, vegetation, river channels, and bare land within the study area as the sample area factors for interpretation training.

#### 4.3 Image interpretation and accuracy assessment

25 Image interpretation and classification were conducted using the Maximum Likelihood module in ERDAS IMAGINE. The interpretation and classification results of the satellite images before and after Typhoon Nanmadol in 2011 and Typhoon Kong-rey in 2013 are shown in Fig. 3. The different colors in the images represent different interpretation factors.

To verify the accuracy of the results, we randomly extracted 25 points from the satellite images for each training factor as checkpoints and tested the accuracy by using the aforementioned error matrix approach. With the satellite images before and

after Typhoon Kong-rey in 2013 as an example, Table 2 shows the error matrix and accuracy assessment results of the satellite image interpretation and classification processes. Table 3 presents the *Kappa* values and *OA* results of the satellite images captured before and after the two typhoons. As mentioned, *Kappa* values ranging from 0.4 to 0.8 indicate moderate accuracy, and thus the interpretation results had moderate to high accuracy.

## 5 5.1 Landslide susceptibility assessment

To evaluate the landslide susceptibility of slopes within the study area, we constructed 8 m × 8 m grids by using the GIS platform along with the interpretation results of the two typhoons. We also constructed an 8 m × 8 m digital elevation model (DEM) and input the classification results, thematic map of predisposing factors, map of the natural environment, and rainfall data into the pixel to aid subsequent landslide susceptibility assessments.

### 10 5.1 Predisposing Impact factor selection and factor correlation test

#### 5.1.1 Predisposing Impact factor selection

Referring to Chen et al. (2009), we divided the predisposing impact factors of landslides into three categories: natural environment, land disturbance, and rainfall.

A. Natural environment factors

#### 15 (A) Elevation

The influence of elevation varies with the climate and thus affects the distribution of vegetation on the slope and type of weathering. In addition, elevation reflects the influence of geological structure, stress, and time. The highest and lowest elevations in the study area were 1480.6 and 365.2 m, respectively. Using the GIS platform, we extracted the elevation data from the DEM of the study area to estimate the mean elevation of each grid. We divided the elevation data into seven classes grades at intervals of 300 m.

(B) Slope gradient

A slope's gradient generally exerts significant impact on slope stability. By using the DEM and gradient analysis of the GIS platform, we calculated the mean gradient of each pixel grid in the study area; subsequently, we divided the gradient values in the pixels grids within the study area into seven classes grades.

#### 25 (C) Aspect

Rainfall-induced landslides are subject to the influence of seasonal changes such as those related to rainfall and wind direction. Thus, the direction of the slope must be considered. As described, we used the DEM and aspect analysis function of the GIS platform to calculate the average aspect of the pixels grids in the study area. According to their direction, we divided them into six classes from windward to flat ground.

#### (D) Geology

Referring to the digital file of the Geologic Map of Taiwan, Scale 1:50,000, Chiahsien, which was compiled by the Central Geological Survey of the Ministry of Economic Affairs in 2000, we determined that the geology of the study area includes five types of rock: the upper part of Changshan Formation, the Tangenshan Formation, the Changchihkeng Formation from the Miocene period, and modern alluvium and terrace deposits from the Holocene period. We divided geological **formations** **strength** into six **classes** **grades** (Chen et al., 2009).

#### (E) Terrain roughness

Terrain roughness refers to the degree of change in **pixel** **grid** height. Wilson and Gallant (2000) proposed the use of the standard deviation of height within a radius to measure the degree of change in height because of its indicative meaning in relation to changes in regional height. Using the **Neighborhood (Focal Statistics) of Spatial Analyst Tools** in ArcGIS, we calculated the terrain roughness of the DEM. Statistical cluster analysis was used to automatically divide terrain roughness into six **classes** **grades**.

#### (F) Slope roughness

Slope roughness refers to the fluctuations in slope gradient in the **pixels** **grids**. High slope roughness means that the slope gradient varies considerably (Wilson and Gallant, 2000). Slope roughness is calculated through the same method as terrain roughness, except with the original elevation values being replaced with the slope gradient values obtained using ArcGIS. Just as terrain roughness was graded, we first used **Spatial Analyst Tools** in ArcGIS to estimate the slope roughness of each **pixel** **grid**, after which we used cluster analysis to automatically divide slope roughness into six **classes** **grades**.

#### (G) Distance to water

**Streams will cause soil erosion and riparian erosion, which directly or indirectly affect the stability of the slope.** We calculated the distances to water using **Tool of Buffer in** ArcGIS and divided the distances into seven **classes** **levels**.

#### (H) Distance to road

**The construction of the roads will also have the influence on the stability of the slope. Therefore,** we also calculated the distances to road using **Tool of Buffer in** ArcGIS and divided the distances into seven **classes** **levels**.

#### 25 B. Land disturbance factors

Land disturbance varies with space and time. **Based on the tendency to promote landslides, the index of land disturbance was developed, and we** made some revisions to the **qualitative** approach proposed by Chen et al. (2009, 2013b) to calculate land disturbance and selected roads, buildings, crops, bare land, and vegetation as the land disturbance factors of landslides in the study area. We extracted the disaster and ground surface data from previous satellite image interpretation and classification results and input the land disturbance factors into the **pixels** **grids** by using the GIS platform. The scores of the index for disturbance condition ( $I_{DC}$ ) in the **pixels** **grids** are shown in Table 4.

#### C. Rainfall factors

We collected precipitation data from weather stations close to the Central Weather Bureau, including Guanshan, Biaohu, Hsiao Guanshan, Gaojhong, Sinfa, Jiasian, and Xi'nan. Table 5 displays the station information. We then calculated the *EAR* and 3-hour  $I_R$  ( $I_{3R}$ ) levels observed at each station. The results from Typhoon Nanmadol in 2011 and Typhoon Kong-rey in 2013 are compiled in Table 6. By using the Inverse Distance Weighting (*IDW*) function of ArcGIS and the *EAR* and maximum  $I_{3R}$  values of the weather stations, we estimated the rainfall of each pixel grid throughout the study area and then used cluster analysis to divide the results into six classes levels.

### 5.1.2 Factor correlation test

To establish a landslide susceptibility assessment model, we selected elevation, slope gradient, aspect, geology, terrain roughness, slope roughness, distance to water, distance to road,  $I_{DC}$ , and rainfall as landslide-predisposing triggering factors. Rainfall included *EAR* and maximum  $I_{3R}$ .

We employed the Pearson correlation test tool in SPSS (2005) to examine the correlation among these factors. The correlation coefficients ranged from -1 to +1, with +1, -1, and 0 indicating complete positive correlation, complete negative correlation, and no correlation between two variables, respectively. Factors with high correlation were then subjected to a paired sample *t* test conducted using SPSS to examine the significance of the correlation between them. Those with high correlation were eliminated.

Table 7 presents the test results regarding the correlation between the predisposing impact factors. As shown, the degree of correlation between most factors was moderate to low. A high degree of correlation was found only between elevation and terrain roughness and between slope gradient and slope roughness. Thus, we administered paired sample *t* tests to these two factor pairs to test the significance of the correlation. The results in Table 8 show that the significance was 0 (<0.05) for the correlation between both pairs, indicating no correlation; thus, these factors were not eliminated.

## 5.2 Landslide susceptibility assessment and hazard map

To apply the MHEM to establish a landslide susceptibility assessment model, we input the natural environment, land disturbance, and rainfall factors into the pixels grids by using the GIS platform. By using the changes in bare land between the images before and after the typhoons and applying image subtraction aided by manual checking, we obtained the pixel grid data of the rainfall-induced landslide locations in the study area. With the study area after Typhoon Nanmadol in 2011 as an example, we considered *EAR* during the rainfall period and rated the classes grades by using the factor weights derived using the MHEM, as shown in Table 9.

The calculation process is explained in this paper by using elevation as an example. In accordance with factor selection, the elevation factor was divided into seven classes grades. Aided by the GIS platform, we calculated the total number of pixels grids, total number of landslides, and landslide percentage within each elevation level in the study area by using Eqs. (8) and (9). Based on the landslide percentages of the elevation factor and the minimum and maximum landslide percentages, we subsequently obtained the scores of the factors by using Eq. (10). We then calculated the standard deviation, coefficient of

variation, and weight values by using Eqs. (11) and (12); the results are listed in Table 9. The presented results show that the standard deviation ( $\sigma$ ), coefficient of variation ( $V$ ), and factor weight ( $W$ ) of landslide percentage were 0.021, 0.764, and 0.087, respectively. Finally, we calculated the instability indices by using the weight values and scores of the factors through Eq. (13). Furthermore, the results in Table 9 indicate that the degrees of land disturbance ( $I_{DC}$ ), geology ( $G_s$ ), slope gradient ( $S_s$ ), and slope roughness had the greatest influence on landslides in the study area, followed by distance to water ( $D_s$ ),  $EAR$ , and elevation ( $E_i$ ).

We considered  $EAR$  and  $I_{3R}$  and used an instability index to determine the level of landslide susceptibility of slopes throughout the study area. The derived instability index intervals (Table 10) ranged from 2.05 (2.02) to 9.59 (9.96). By using Eqs. (14) and (15), the landslide probability intervals calculated based on  $EAR$  and  $I_{3R}$  are presented in Table 10. We employed the mean probability of landslide occurrence to differentiate between high and low landslide susceptibility. Landslides were considered more likely to occur in areas where the probability of landslide occurrence was greater than the mean. By contrast, landslides were considered less likely to occur in areas where the probability of landslide occurrence was lower than the mean. With rainfall factor  $EAR$  as an example, we determined the mean probability of landslide occurrence to be 0.46. We further divided landslide susceptibility into four levels: high (0.731–1), medium high (0.461–0.73), medium low (0.23–0.46), and low (0–0.23). The results showed that the mean probability of landslide occurrence varied little, regardless of whether it was calculated using  $EAR$  or  $I_{3R}$ .

By using the GIS platform, we considered the landslide susceptibility calculated using  $EAR$  for Typhoon Nanmadol in 2011 as an example. As illustrated in Fig. 4, we included an overlay created by the NCDR and showing the locations of historical disasters within the study area. The results revealed a total of 24 historical disasters, 17 of which were situated in areas of medium high or high landslide susceptibility. Therefore, the estimation accuracy in this study was approximately 71%. Regarding Typhoon Kong-rey in 2013, 18 historical disasters occurred within areas of medium high or high landslide susceptibility, thereby yielding 75% accuracy. Table 11 presents the accuracy levels associated with using different rainfall factors to calculate landslide susceptibility for different typhoons.

### 5.3 Investigation of rainfall factors and instability index

To understand the relationship between the rainfall factors and the degree of instability on the slopes in the study area after typhoons, we first removed the cloud cover grids from post typhoon images and subsequently employed cluster analysis to divide the instability indices of the pixels grids into three levels: high, medium, and low. We then collected random samples based on the proportions of landslide and non-landslide pixels grids in each level (50 landslide and 50 non-landslide pixel grid points) and plotted their relationship. Table 12 and Fig. 5a–d present the relationships between the rainfall factors ( $EAR$  and  $I_{3R}$ ), instability index, and landslide occurrence in the pixels grids following Typhoon Nanmadol in 2011 and Typhoon Kong-rey in 2013. Figure 5a and b consider  $EAR$ , whereas Fig. 5c and d consider  $I_{3R}$ . The presented results indicate that the typhoon events increased the degree of slope instability ( $D_i$ ) and landslide occurrence, regardless of whether  $EAR$  or  $I_{3R}$  was considered. Furthermore, significantly more landslide points were situated in areas of high instability than in areas of other

levels of instability, and landslides rarely occurred in areas of low instability. Moreover, areas of high slope instability were prone to landslides even if their  $EAR$  or  $I_{3R}$  was low. By contrast, areas of low instability required more rainfall for landslides to be possible. The results (Table 12) further showed that the  $EAR$  and  $I_{3R}$  levels of Typhoon Kong-rey in 2013 were greater than those of Typhoon Nanmadol in 2011. Thus, in any  $D_i$  level, the proportion of landslides that occurred in the study area after Typhoon Kong-rey was higher than that after Typhoon Nanmadol. Figure 5e and f present the relationships between  $EAR \times I_{3R}$ , the instability index, and landslide occurrence;  $EAR \times I_{3R}$  is the index of rainfall-induced landslide (ILR), with a higher value indicating higher susceptibility to a landslide. The figures show that for a high instability index, even a small rainfall event could trigger a landslide (lower right corners of the figures). By contrast, for a low instability index, a larger rainfall event could not easily trigger a landslide (upper left corners of the figures).

## 10 6 Landslide location analysis

We analyzed the spatial characteristics of landslides by using landslide locations collected from before and after both of the two typhoons and the land surface interpretation results of the study area.

### 6.1 Investigation of landslide predisposing impact factors and landslide area

The influence of predisposing causal factors on landslides varies. In this study, we examined the relationships between landslide area and various predisposing landslide factors. By using the area of landslides (i.e., the number of landslide pixels grids) induced by Typhoon Nanmadol in 2011 as an example, we investigated the influences of the predisposing causal factors (elevation, slope gradient, aspect, geology, slope roughness, terrain roughness, distance to water, distance to road, and degree of land disturbance) on landslides. The various factor classes levels and corresponding numbers of landslide pixels grids are shown in Fig. 6a–i.

Figure 6a presents the relationship between different classes levels of elevation and the number of landslide pixels grids (landslide area). As shown in the figure, the number of landslide pixels grids in the study area peaked at elevations between 450 and 750 m and then declined as the elevation increased. Figure 6b displays the relationship between different classes levels of slope gradient and the number of landslide pixels grids (landslide area). As shown in the figure, the number landslide pixels grids in the study area increased with the slope gradient and peaked between  $30^\circ$  and  $55^\circ$ . Landslides rarely occurred on slopes steeper than  $55^\circ$ . Figure 6c illustrates the relationship between aspect and the number of landslide pixels grids, with aspect divided into eight categories: north, northeast, east, southeast, south, southwest, west, and northwest. As shown in the figure, the number of landslide pixels grids was highest on slopes facing south, followed by those on slopes facing east and southeast. We speculate that this is because rainfall during the typhoon season in Taiwan promotes poor cementation and high weathering on slopes along rivers, which consequently prompts these slopes to develop toward low-lying rivers (which run from the northeast to the southwest) after rainfall events.

Figure 6d shows the relationship between geology and the number of landslide pixels grids. As shown in the figure, the Sanhsia Group and its stratigraphic equivalence lead to landslides more easily than does the Lushan Formation in the study area. The Sanhsia Group and its stratigraphic equivalence mainly comprise sandstone, shale, and interbedded sandstone and shale. Shale has weaker cementation, lower strength, and a greater tendency to weather and fracture. By contrast, the Lushan Formation consists of argillite, slate, and interbedded argillite and sandstone, and its strength is controlled by cleaving; some areas are prone to weathering and fracturing. Thus, both rock types are more likely to collapse, but on the whole, the Sanhsia Group and its stratigraphic equivalence collapse more easily than does the Lushan Formation. Furthermore, this result indicates that the locations of landslide areas within the study area are associated with geology. Figure 6e presents the relationship between slope roughness and the number of landslide pixels grids. The number of landslide pixels grids within a level of slope roughness first increased with the slope roughness and then began to decline once a certain level of slope roughness (35–40) was reached. This result is similar to that of the influence of slope gradient on the number of landslide pixels grids. Figure 6f displays the relationship between terrain roughness and the number of landslide pixels grids. As shown in this figure, the results are similar to those regarding the influence of elevation on the number of landslide pixels grids; the number of pixels grids declined when the terrain roughness was greater than 500 and was very small low the terrain roughness was greater than 1200.

Figure 6g illustrates the relationship between distance to water and the number of landslide pixels grids. The presented results show a significantly greater number of landslide pixels grids within 300 m of water. The width of the river channel within the study area was determined to range from 100 to 200 m, revealing that the development of landslide areas near water in the study area is caused by rainfall significantly raising the water level in the river, which scours the slope toe, affects slope stability, and triggers landslides. Figure 6h presents the relationship between distance to road and the number of landslide pixels grids. The presented results reveal that areas between 100 and 300 m from roads had the greatest number of landslide pixels grids. Further examination of the relationship between distance to road and the area and number of landslides revealed that most landslides between 0 and 100 m from roads were small collapses, whereas those between 100 and 300 m from roads were larger in area. The number of landslides 0–100 m from roads was greater than that 100–300 m from roads.

The degree of land disturbance can represent the changes of surface conditions including roads, buildings, crops, bare land, and vegetation. A greater degree of land disturbance likely indicates a greater degree of surface changes, which can yield a greater number of landslide pixels grids. Figure 6i shows the relationship between the degree of land disturbance and the number of landslide pixels grids. The presented results indicate that the number of landslide pixels grids increased with the degree of land disturbance.

## 6.2 Landslide scale and spatial distribution

We employed the terrain tool in ERDAS IMAGINE and the DEM to identify the ridges and valleys in the study area. Following the methods in previous studies (Meunier et al., 2008; Chue et al., 2015), we extracted the distances between the

highest point of a landslide area and the nearest ridge ( $dr$ ), between the lowest point of the landslide area and the nearest stream ( $ds$ ), and between the ridge and the stream ( $dt$ ) (Fig. 7). Furthermore, in Taiwan, many slopes are visible on developed, mountain roads built between ridges and streams. Therefore, we explored the spatial distribution of landslides above and below mountain roads. Similar to Fig. 7a, to explore the spatial distribution of landslides, we extracted the distances between the highest point of a landslide area on a slope above a road and the nearest ridge ( $dr$ ), between the lowest point of the landslide area and the nearest mountain road ( $dmu$ ), and between the ridge and the mountain road ( $dtu$ ) (Fig. 7b); we also investigated this distribution by extracting the distances between the highest point of a landslide area on a slope below a road and the nearest mountain road ( $dmd$ ), between the lowest point of the landslide area and the nearest stream ( $ds$ ), and between the mountain road and the stream ( $dtd$ ) (Fig. 7c).

This study examined the spatial distribution of landslides in the region along Provincial Highway No. 20 before and after Typhoon Nanmadol in 2011 and Typhoon Kong-rey in 2013. Using the approach shown in Fig. 7a, we mapped the bare land in the study area, as shown in Fig. 8a–d. Of these figures, Fig. 8a and c show the conditions before the typhoons, whereas Fig. 8b and d present the conditions after the typhoons. The presence of bare locations near the Y axis ( $dr/dt \approx 0$ ) denotes that the bare land originated near the ridge. By contrast, the presence of bare locations near the X axis ( $ds/dt \approx 0$ ) denotes that the bare land progressed toward the stream. Thus, the presence of bare locations near the origin denotes that the bare land originated near the ridge and progressed toward the stream.

The results in Fig. 8a–d show more bare locations in the lower right halves of the graphs, some of which are larger in area. The figures indicate fewer bare locations in the upper left halves of the graphs, and the ones that are present are smaller in area. These spatial distribution characteristics are similar to those derived by Meunier et al. (2008). We speculate that this is because the frequency of rainfall-induced landslides increases significantly because of bank erosion, which is shown in the lower right half of Fig. 8 ( $dr/dt \geq 0.5$  and  $ds/dt \leq 0.5$ ). Furthermore, the bare locations before and after Typhoons Nanmadol and Kong-rey show that the bare land does not increase in number but increases significantly in area, implying that old landslides may result in more collapses or expansions of the affected area. In addition, the number of old landslides is greater than that of new landslides.

We explored the spatial distribution of landslides on slopes above (Fig. 9) and below (Fig. 10) mountain roads in the study area before and after Typhoon Kong-rey in 2013. Figure 9a and Fig. 10a present the spatial distribution of bare land before the typhoon, whereas Fig. 9b and Fig. 10b present the spatial distribution of bare land after the typhoon.

As shown in Fig. 9, most landslides on the slopes above the mountain roads occurred close to the roads, most likely because road construction involves cutting the slope toe and increasing the gradient. After the typhoon, the bare locations on the slopes above the roads in the study area did not increase in number significantly; thus, rainfall did not exert a substantial impact on the slopes above the roads. The results in Fig. 10 show bare locations on the slopes below the mountain roads developing from near the roads to the streams. The bare locations near the streams may also have been affected by rainfall-induced bank erosion. However, the bare land near the roads may have been a result of roads being constructed in the study area, which affects slope stability and increases the probability of landslides. Furthermore, the bare locations near the roads



slightly increased in number after the typhoon, likely because the roads changed the routes of surface runoff. The area of bare land near the streams also increased, possibly because the water flow scours the slope toe and causes continual bank collapses. Thus, typhoons have a significant impact on the stability of slopes below mountain roads.

## 7 Conclusions

5 This study applied the maximum likelihood method to interpret and classify satellite images before and after two typhoons in 2011 and 2013. We extracted landslide and land use information from the areas surrounding roads and then compiled the rainfall and DEM data from the typhoon events. By using the MHEM, we established a landslide susceptibility assessment model and examined the relationships between predisposing ~~causal~~ factors and the area and number of landslides within the study area, as well as the relationships between roads and the spatial distribution of landslides. The results show that the

10 *Kappa* coefficients associated with the use of the maximum likelihood method to interpret and classify satellite images before and after Typhoon Nanmadol in 2011 and Typhoon Kong-rey in 2013 ranged from 0.53 to 0.66, whereas the *OA* ranged from 61% to 71%, indicating moderately high accuracy. According to the results of the instability index-based landslide susceptibility assessment model, the degree of land disturbance, geology, slope gradient, and slope roughness had the greatest impacts on landslides. A comparison of historical landslides triggered by the typhoons and the results of the

15 hazard map revealed 71% accuracy for Typhoon Nanmadol in 2011 and 75% accuracy for Typhoon Kong-rey in 2013. Regarding the influence of the predisposing ~~causal~~ factors, an elevation of 450–750 m, a slope gradient of 30°–55°, and distances within 300 m of water or roads were associated with a larger scale of landslides. The scale of landslides also increased with the degree of land disturbance. The relationships between the ILR, instability index, and landslide occurrence indicate that for a high instability index, even a smaller rainfall event could trigger a landslide. By contrast, for a low

20 instability index, a larger rainfall event could not easily trigger a landslide. Thus, the instability index can effectively reflect landslide susceptibility. Comparisons of the distribution of bare land before and after typhoon events showed that most landslides in the study area were caused by stream water scouring away the toes of bank slopes. Although bare locations did not significantly increase in number after the typhoon events, they increased significantly in area, implying that the number of old landslide areas holding more collapses or expansions was greater than that of new landslide areas developing. In

25 addition, the results obtained from observing changes in slopes above and below mountain roads after the typhoon events indicate that the number of bare locations on the slopes above the roads in the study area did not increase significantly, whereas the bare locations near the roads on the slopes below the roads slightly increased in number after the typhoon events, likely because of the roads changing the routes of surface runoff. The amount of bare land near streams also increased, possibly because the water flow scours the slope toe.

## References

- Ali, A., Huang, J., Lyamin, A. V., Sloan, S. W. and Cassidy, M. J.: Boundary effects of rainfall-induced landslides, *Computers and Geotechnics*, 61, 351-354, 2014.
- Anbalagan, D.: Landslide hazard evaluation and zonation mapping in mountainous terrain, *Engineering Geology*, 32, 269–277, 1992.
- 5 Akgün, A., Dag, S., and Bulut, F.: Landslide susceptibility mapping for a landslide prone area (Findikli, NE of Turkey) by likelihood-frequency ratio and weighted linear combination models, *Environ. Geol*, 54, 1127–1143, 2008.
- Ayalew, L., and Yamagishi, H.: The application of GIS-based logistic regression for landslide susceptibility mapping in the Kakuda–Yahiko Mountains, Central Japan, *Geomorphology*, 65, 15–31, 2005.
- 10 Ayalew, L., Yamagishi, H., Marui, H., and Kanno, T.: Landslides in Sado Island of Japan: Part II. GIS-based susceptibility mapping with comparisons of results from two methods and verifications, *Eng. Geol*, 81, 432–445, 2005.
- Baeza, C. and Corominas, J.: Assessment of shallow landslide susceptibility by means of multivariate statistical techniques, *Earth Surface Processes and Landforms*, 26(12), 1251-1263, doi: 10.1002/esp.263, 2001.
- Bai, S. B., Wang, J., Lu, G. N., Zhou, P. G., Hou, S. S., and Xu, S. N.: GIS-based and data-driven bivariate landslide susceptibility mapping in the Three George area, China. *Pedosphere*, 19, 14–20, 2009.
- 15 Barredo, J. I., Benavides, A., Hervas, J., and vanWesten, C. J.: Comparing heuristic landslide hazard assessment techniques using GIS in the Tirajana basin, Gran Canaria Island, Spain. *Int. J. Appl. Earth Obs. Geoinf.*, 2, 9–23, 2000.
- Brabb, E. E.: Innovative approaches to landslide hazard and risk mapping, *Proceedings of the Fourth International Symposium on Landslides*, Canadian Geotechnical Society, Toronto, Canada. 1:307–324, 1984.
- 20 Bruzzone, L and Prieto, D. F.: Unsupervised retraining of a maximum likelihood classifier for the analysis of multitemporal remote sensing images, *IEEE Transactions on Geoscience and Remote Sensing* 39(2), 456-460, doi: 10.1109/36.905255, 2001.
- Carrara, A., Crosta, G., and Frattini, P.: Geomorphological and historical data in assessing landslide hazard. *Earth Surf. Process. Landf.* 28, 1125–1142, 2003.
- 25 Carrara, A., Crosta, G., and Frattini, P.: Comparing models of debris-flow susceptibility in the alpine environment, *Geomorphology*, 94, 353–378, 2008.
- Central Weather Bureau (CWB), Ministry of Transportation and Communications (MOTC), Executive Yuan, R.O.C. (Taiwan), <http://www.cwb.gov.tw/V7/knowledge/encyclopedia/ty038.htm>, 2017. (in Chinese)
- Chadwick, J., Dorsch, S., Glenn, N., Thackray, G., and Shilling, K.: Application of multi-temporal high-resolution imagery and GPS in a study of the motion of a canyon rim landslide, *ISPRS, Journal of Photogrammetric Engineering and Remote Sensing*, 59(4), 212-221, 2005.
- 30 Chang, K. T., Chiang, S. H. and Lei F.: Analysing the Relationship between Typhoon-Triggered Landslides and Critical Rainfall Conditions, *Earth Surface Processes and Landforms*, 33, 1261-1271, 2007.

- Chen, C. Y., Chen T. C., Yu F. C., Yu W. H., Tseng C. C.: Rainfall duration and debris-flow initiated studies for real-time monitoring, *Environ. Geol.*, 47, 715–724, DOI 10.1007/s00254-004-1203-0, 2005.
- Chen, J. W., Chue, Y. S and Chen, Y. R.: The Application of Genetic Adaptive Neural Network in Landslide Disaster Assessment, *Journal of Marine Science and Technology*, 21(4), 442-452. doi: 10.6119/JMST-012-0709-2, 2013a.
- 5 Chen, L., Wei, H. P., and Chen, H. M.: A Study of Applying Supervised Classifications for Remote Sensing Imagery Recognition Techniques, *Journal of Taiwan Agricultural Engineering*, 50(3), 59-70, 2004. (in Chinese)
- Chen, Y. R., Chen, J. W., Hsieh, S. C., and Ni, P. N.: The application of remote sensing technology to the interpretation of land use for rainfall-induced landslides based on genetic algorithms and artificial neural networks, *IEEE Journal of Selected Topics in Applied Earth Observations and Remote Sensing*, 2(2), 87-95. doi: 10.1109/JSTARS.2009.2023802, 10 2009.
- Chen, Y. R., Ni, P. N., and Tsai, K. J.: Construction of a sediment disaster risk assessment model, *Environmental Earth Sciences*, 70(1), 115-129. doi: 10.1007/s12665-012-2108-y, 2013b.
- Chue, Y. S., Chen, J. W., and Chen, Y. R.: Rainfall-induced slope landslide potential and landslide distribution characteristics assessment, *Journal of Marine Science and Technology*, 23(5), 705-716, doi: 10.6119/JMST-015-0529-3, 15 2015.
- Cohen, J.: A coefficient of agreement for nominal scales, *Educ. Psychol. Meas.*, 20, 37–46, doi: 10.1177/001316446002000104, 1960.
- Congalton, R. G.: A review of assessing the accuracy of classifications of remotely sensed data, *Remote Sensing of Environment*, 37(1), 35-46, doi: 10.1016/0034-4257(91)90048-B, 1991.
- 20 Constantin, M., Bednarik, M., Jurchescu, M. C., and Vlaicu, M.: Landslide susceptibility assessment using the bivariate statistical analysis and the index of entropy in the Sibiciu Basin (Romania), *Environ. Earth Sci.*, 63(2), 397–406, 2011.
- Crozier, M. J., and Eyles, R. J.: Assessing the probability of rapid mass movement, In *The New Zealand Institution of Engineers—Proceedings of Technical Groups* (ed.), Proc. Third Australia–New Zealand Conference on Geomechanics, Wellington, 2.47–2.51, 1980.
- 25 Dadson S. J., Hovius N., Chen H., Dade W. B., Lin J. C., Hsu M. L., Lin C.W., Horng M. J., Chen T. C., Milliman J., and Stark C. P.: Earthquake triggered increase in sediment delivery from an active mountain belt, *Geology*, 32(8), 733–736, doi: 10.1130/G20639.1, 2004.
- Dai, F. C. and Lee, C. F.: Frequency-volume relation and prediction of rainfall-induced landslides, *Engineering Geology*, 59(3-4), 253-266, doi: 10.1016/S0013-7952(00)00077-6, 2002.
- 30 Das, I., Sahoo, S., Westen, C., Stein, A., and Hack, R.: Landslide susceptibility assessment using logistic regression and its comparison with a rock mass classification system, along a road section in the northern Himalayas (India), *Geomorphology*, 114, 627–637, 2010.
- Das, I., Stein, A., Kerle, N., and Dadhwal, V. K.: Landslide susceptibility mapping along road corridors in the Indian Himalayas using Bayesian logistic regression models, *Geomorphology*, 179, 116–125, 2012.

- Devkota, K. C., Regmi, A. D., Pourghasemi, H. R., Yoshida, K., Pradhan, B., Ryu, I. C., Dhital, M. R., and Althuwaynee, O. F.: Landslide susceptibility mapping using certainty factor, index of entropy and logistic regression models in GIS and their comparison at Mugling–Narayanghat road section in Nepal Himalaya, *Nat. Hazards*, 65, 135–165, DOI 10.1007/s11069-012-0347-6, 2013.
- 5 Erbek, S. F., Ozkan, C., and Taberner, M.: Comparison of maximum likelihood classification method with supervised artificial neural network algorithms for land use activities, *International Journal of Remote Sensing*, 25(9), 1733–1748, doi: 10.1080/0143116031000150077, 2004.
- Fernandez, C. I., Castillo, T. F., Hamdouni, R. E., and Montero, J. C.: Verification of landslide susceptibility mapping: a case study, *Earth Surface Processes and Landforms*, 24, 537–544, doi: 10.1002/(SICI)1096-  
10 9837(199906)24:6<537:AID-ESP965>3.0.CO;2-6, 1999.
- Gianneccini, R.: Relationship between rainfall and shallow landslides in the southern Apuan Alps (Italy), *Nat. Hazards Earth Syst. Sci.*, 6, 357–364, <https://doi.org/10.5194/nhess-6-357-2006>, 2006.
- Gianneccini, R., Galanti, Y., and D'Amato Avanzi, G.: Critical rainfall thresholds for triggering shallow landslides in the Serchio River Valley (Tuscany, Italy), *Nat. Hazards Earth Syst. Sci.*, 12, 829–842, [https://doi.org/10.5194/nhess-12-829-2012](https://doi.org/10.5194/nhess-12-<br/>15 829-2012), 2012.
- Gökçeoglu, C., and Aksoy, H.: Landslide susceptibility mapping of the slopes in the residual soils of the Mengen region (Turkey) by deterministic stability analyses and image processing techniques, *Engineering Geology*, 44, 147–161, 1996.
- Greco, R., Sorriso-Valvo, M., and Catalano, E.: Logistic regression analysis in the evaluation of mass movements susceptibility: the Aspromonte case study, Calabria, Italy, *Eng. Geol.*, 89, 47–66, 2007.
- 20 Guimarães, R. F., Montgomery, D. R., Greenberg, H. M., Fernandes, N. F., Gomes, R., and Abilio deCarvalho Júnior O.: Parameterization of soil properties for a model of topographic controls on shallow landsliding: application to Rio de Janeiro, *Engineering Geology*, 69, 99–108, 2003.
- Gupta, R. P., and Anbalagan, R.: Slope stability of Theri dam reservoir area, India, using landslide hazard zonation (LHZ) mapping. *Q J Eng. Geol.*, 30, 27–36, 1997.
- 25 Guzzetti, F., Carrara, A., Cardinali, M., and Reichenbach, P.: Landslide hazard evaluation: an aid to a sustainable development, *Geomorphology*, 31, 181–216, 1999a.
- Guzzetti, F., Carrara, A., Cardinali, M., and Reichenbach, P.: Landslide hazard evaluation: a review of current techniques and their application in a multi-scale study, Central Italy. *Geomorphology* 31, 181–216, 1999b.
- Guzzetti, F., Reichenbach, P., Cardinali, M., Galli, M., and Ardizzone, F.: Probabilistic landslide hazard assessment at the  
30 basin scale, *Geomorphology*, 72(1-4), 272–299, <https://doi.org/10.1016/j.geomorph.2005.06.002>, 2005.
- Hammond, C., Hall, D., Miller, S., and Swetik, P.: Level I Stability Analysis (LISA) Documentation for Version 2.0. General Technical Report INT-285, USDA Forest Service Intermountain Research Station, 1992.
- Jiang, H., and Eastman, J. R.: Application of fuzzy measures in multi-criteria evaluation in GIS, *Int. J. Geogr. Inf. Sci.*, 14, 173–184, 2000.

- Iverson, R. M.: Landslide triggering by rain infiltration, *Water Resource Research*, 36, 1897–1910, 2000.
- Kamp, U., Growley, B. J., Khattak, G. A., and Owen, L. A.: GIS-based landslide susceptibility mapping for the 2005 Kashmir earthquake region, *Geomorphology*, 101, 631–642, 2008.
- 5 Kanungo, D. P., Arora, M. K., Sarkar, S., and Gupta, R. P.: A comparative study of conventional, ANN black box, fuzzy and combined neural and fuzzy weighting procedures for landslide susceptibility zonation in Darjeeling Himalayas, *Eng. Geol.*, 85, 347–366, 2006.
- Kayastha, P., Dhital, M. R. and De Smedt, F.: Application of the analytical hierarchy process (AHP) for landslide susceptibility mapping: A case study from the Tinau watershed, west Nepal, *Computers & Geosciences*, 52, 398-408, <http://dx.doi.org/10.1016/j.cageo.2012.11.003>, 2013.
- 10 Landis, J. R. and Koch, G. G.: The measurement of observer agreement for categorical data, *Biometrics*, 33(1), 159-174. doi: 10.2307/2529310, 1977.
- Lee, S., Ryu, J., Won, J., and Park, H.: Determination and application of the weight for landslide susceptibility mapping using an artificial neural network, *Eng. Geol.*, 71, 289–302, 2004.
- Lee, C. T., Huang, C. C., Lee, J. F., Pan, K. L., Lin, M. L., and Dong, J. J.: Statistical approaches to storm event-induced landslide susceptibility, *Natural Hazard and Earth system Sciences*, 8, 941-960, doi: 10.1016/j.enggeo.2008.03.004, 2008.
- 15 Li, Y., Chen, G., Tang, C., Zhou, G., and Zheng, L.: Rainfall and earthquake-induced landslide susceptibility assessment using GIS and Artificial Neural Network, *Nat. Hazards Earth Syst. Sci.*, 12, 2719-2729, <https://doi.org/10.5194/nhess-12-2719-2012>, 2012.
- 20 Lillesand, T. M., Kiefer, R. W., and Chipman, J. W.: *Remote Sensing and Image Interpretation*, New York: John Wiley & Sons, ISBN 978-1-118-34328-9, 2004.
- Lin, C. W., Shieh, C. J., Yuan, B. D., Shieh, Y. C., Huang, M. L., and Lee, S. Y.: Impact of Chi-Chi earthquake on the occurrence of landslides and debris flows: example from the Chenyulan River watershed, Nantou, Taiwan, *Engineering Geology* 71(1-2), 49–61, [https://doi.org/10.1016/S0013-7952\(03\)00125-X](https://doi.org/10.1016/S0013-7952(03)00125-X), 2004.
- 25 Lin, C. W., Liu, S. H., Lee, S. Y., and Liu, C. C.: Impacts of the Chi-Chi earthquake on subsequent rainfall-induced landslides in central Taiwan, *Engineering Geology* 86(2-3), 87-101, <https://doi.org/10.1016/j.enggeo.2006.02.010>, 2006.
- Lin, C. W., Chang, W. S., Liu, S. H., Tsai, T. T., Lee, S. P., Tsang, Y. C., Shieh, C. L., and Tseng, C. M.: Landslides Triggered by the 7 August 2009 Typhoon Morakot in Southern Taiwan, *Engineering Geology*, 123(1-2), 3–12, <https://doi.org/10.1016/j.enggeo.2011.06.007>, 2011.
- 30 Lin, W. T, Chou, W. C., Lin, C. Y., Huang, P. H., and Shyan, T. J.: Vegetation recovery monitoring and assessment at landslides caused by earthquake in Central Taiwan, *Forest Ecology and Management*, 210(1-3), 55-66, doi: 10.1016/j.foreco.2005.02.026, 2005.
- Lin, F. L., Lin, J. R., and Lin, Z. Y.: A zonation technique for landslide susceptibility in watershed, *Journal of Chinese Soil and Water Conservation*, 40(4), 438-453, 2009. (in Chinese)

- Liu, C. C., Liu, J. G., Lin, C. W., Wu, A. M., Liu, S. H., and Shieh, C. L.: Image processing of FORMOSAT-2 data for monitoring South Asia tsunami, *International Journal of Remote Sensing*, 28, 3093-3111, <http://dx.doi.org/10.1080/01431160601094518>, 2007.
- Liu, H. Y., Gao, J. X., and Li, Z. G.: The advances in the application of remote sensing technology to the study of land covering and land utilization, *Remote Sensing for Land and Resources*, 4, 7-12, 2001.
- 5 Martinović, K., Gavin, K., and Reale, C.: Development of a landslide susceptibility assessment for a rail network, *Engineering Geology*, 215, 1–9, 2016.
- Meunier, P., Hovius, N., and Haines, J. A.: Topographic site effects and the location of earthquake induced landslides, *Earth and Planetary Science Letters*, 275, 221-232, doi:10.1016/j.epsl.2008.07.020, 2008.
- 10 Montgomery, D. R., and Dietrich, W. E.: A physically based model for the topographic control on shallow landsliding, *Water Resources Research*, 30, 1153–1171, 1994.
- National Science and Technology Center for Disaster Reduction (NCDR), Executive Yuan, R.O.C. (Taiwan), <https://den.ncdr.nat.gov.tw/Search>, 2017. (in Chinese)
- Nikolakopoulos, K. G., Vaiopoulos, D. A., Skianis, G. A., Sarantinos, P., and Tsitsikas, A.: Combined use of remote sensing, GIS and GPS data for landslide mapping, *Geoscience and Remote Sensing Symposium, IGARSS '05 Proceedings, IEEE international*, 5196-5199, doi I: 10.1109/IGARSS.2005.1526855, 2005.
- 15 Ohlmacher, G. C. and Davis, J. C.: Using multiple logistic regression and GIS technology to predict landslide hazard in northeast Kansas, USA, *Engineering Geology*, 69(3-4), 331-343, DOI:10.1016/S0013-7952(03)00069-3, 2003.
- Okimura, T., and Kawatani, T.: Mapping of the potential surface-failure sites on granite slopes. In: Gardiner E. (ed). *20 International Geomorphology 1986 Part I*, Wiley, Chichester, 121–138, 1987.
- Otukei, J. R. and Blaschke, T.: Land cover change assessment using decision trees, support vector machines and maximum likelihood classification algorithms, *International Journal of Applied Earth Observation and Geoinformation*, 12(1), S27-S31, doi: 10.1016/j.jag.2009.11.002, 2010.
- Pack, R. T., Tarboton, D. G., and Goodwin, C. N.: Gis-based landslide susceptibility mapping with SINMAP. In: Bay JA (ed). *25 Proceedings of the 34th Symposium on Engineering Geology: Logan, Utah State University, Utah*, 219–231, 1999.
- Pantelidis, L.: A critical review of highway slope instability risk assessment systems, *Bull Eng. Geol. Environ.*, 70, 395–400, DOI 10.1007/s10064-010-0328-5, 2011.
- Pellicani, R., Frattini, P., and Spilotro, G.: Landslide susceptibility assessment in Apulian Southern Apennine: heuristic vs. statistical methods, *Environ. Earth. Sci*, 72, 1097–1108, DOI 10.1007/s12665-013-3026-3, 2014.
- 30 Pellicani, R., Spilotro, G., and Van Westen, C. J.: Rockfall trajectory modeling combined with heuristic analysis for assessing the rockfall hazard along the Maratea SS18 coastal road (Basilicata, Southern Italy), *Landslides*, 13, 985–1003, DOI 10.1007/s10346-015-0665-3, 2016.

- Pellicani, R., Argentiero, I., and Spilotro, G.: GIS-based predictive models for regional-scale landslide susceptibility assessment and risk mapping along road corridors, *Geomatics, Natural Hazards and Risk*, DOI: 10.1080/19475705.2017.1292411, 2017.
- Saaty, T. L.: *The Analytical Hierarchy Process*, McGraw Hill, New York, 1980.
- 5 Seo K. and Funasaki, M.: Relationship between sediment disaster (mainly debris flow damage) and rainfall, *International Journal of Erosion Control Engineering*, 26(2), 22-28, 1973.
- Soil and Water Conservation Bureau (SWCB), Council of Agriculture (COA), Executive Yuan, R.O.C. (Taiwan), <http://en.swcb.gov.tw/content/index.aspx?Parser=1,5,23>, 2012.
- SPSS Inc.: *SPSS 14.0 Brief Guide*, SPSS Inc., Chicago. ISBN 0-13-173847-X, 2005.
- 10 Stevenson, P. C.: An empirical method for the evaluation of relative landslide risk, *Bull. Int. Assoc. Eng. Geol.* 16, 69–72, 1977.
- Su, M. B., Tsai, H. S., and Jien, L. B.: Quantitative assessment of hillslope stability in a watershed, *Journal of Chinese Soil and Water Conservation*, 29(2), 105–114, 1998. (in Chinese)
- Sützen, M. L., and Doyuran, V.: Data driven bivariate landslide susceptibility assessment using geographical information systems: a method and application to Asarsuyu catchment, Turkey, *Eng. Geol.*, 71, 303–321, 2004.
- 15 Thiery, Y., Malet, J. P., Sterlacchini, S., Puissant, A., and Maquaire, O.: Landslide susceptibility assessment by bivariate methods at large scales: application to a complex mountainous environment, *Geomorphology*, 92, 38–59, 2007 .
- Van Westen, C. J., Rengers, N., and Soeters, R.: Use of geomorphological information in indirect landslide susceptibility assessment, *Nat Hazards*, 30, 399–419, 2003.
- 20 Van Westen, C. J., Castellanos, E., and Kuriakose, S. L.: Spatial data for landslide susceptibility, hazard, and vulnerability assessment: an overview, *Engineering Geology*, 102(3-4), 112–131, 2008.
- Verbyla, D. L.: *Satellite Remote Sensing of Natural Resources*, New York: CRC Press, ISSN 1-55670-107-4, 1995.
- Wang, H. B. and Sassa, K.: Rainfall-induced landslide hazard assessment using artificial neural networks, *Earth Surface Processes and Landforms*, 31(2), 235-247, doi: 10.1002/esp.1236, 2006.
- 25 Water Resources Agency (WRA), Ministry of Economic Affairs (MOEA), Executive Yuan, R.O.C. (Taiwan), <http://www.wra.gov.tw/ct.asp?xItem=48083&CtNode=8950>, 2017. (in Chinese)
- Wilson, J. P. and Gallant, J. C.: *Terrain analysis-principles and application*, New York: John Wiley & Sons, ISBN 0-471-32188-5, 2000.
- Wu, W., and Siddle, R. C.: A distributed slope stability model for steep forested basins, *Water Resources Research*, 31, 2097–2110, 1995.
- 30 Xie, M. W., Esaki, T., and Zhou, G. Y.: GIS-based probabilistic mapping of landslide hazard using a three-dimensional deterministic model, *Natural Hazards*, 33, 265–282, 2004.
- Yalcin, A.: GIS-based landslide susceptibility mapping using analytical hierarchy process and bivariate statistics in Ardesen (Turkey): comparisons of results and confirmations, *Catena*, 72, 1–12, 2008.

- Yesilnacar, E., and Topal, T.: Landslide susceptibility mapping: a comparison of logistic regression and neural networks methods in a medium scale study, Hendek region (Turkey), *Engineering Geology*, 79(3–4), 251–266, 2005.
- Yilmaz, C., Topal, T., and Suzen, M. L.: GIS-based landslide susceptibility mapping using bivariate statistical analysis in Devrek (Zonguldak-Turkey), *Environ Earth Sci.*, 65(7), 2161–2178, 2012.
- 5 Yoshimatsu, H. and Abe, S.: A review of landslide hazards in Japan and assessment of their susceptibility using an analytical hierarchic process (AHP) method, *Landslide*, 3, 149-158, doi: 10.1007/s10346-005-0031-y, 2006.
- Zhang, G., Cai, Y., Zheng, Zhen, Z., J. Liu, Y., and Huang, K.: Integration of the Statistical Index Method and the Analytic Hierarchy Process technique for the assessment of landslide susceptibility in Huizhou, China, *Catena*, 142, 233-244, <http://dx.doi.org/10.1016/j.catena.2016.03.028>, 2016.



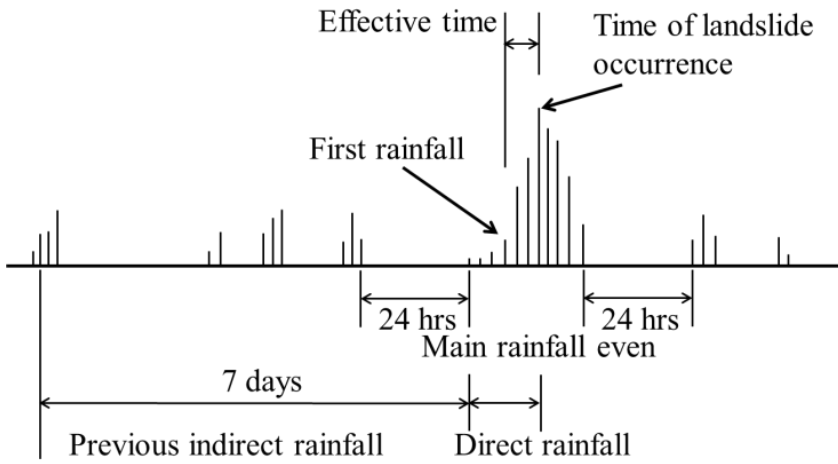


**Figure 1: Definition of Rainfall Events based on Effective Accumulated Rainfall (modified from Seo and Funasaki, 1973)**

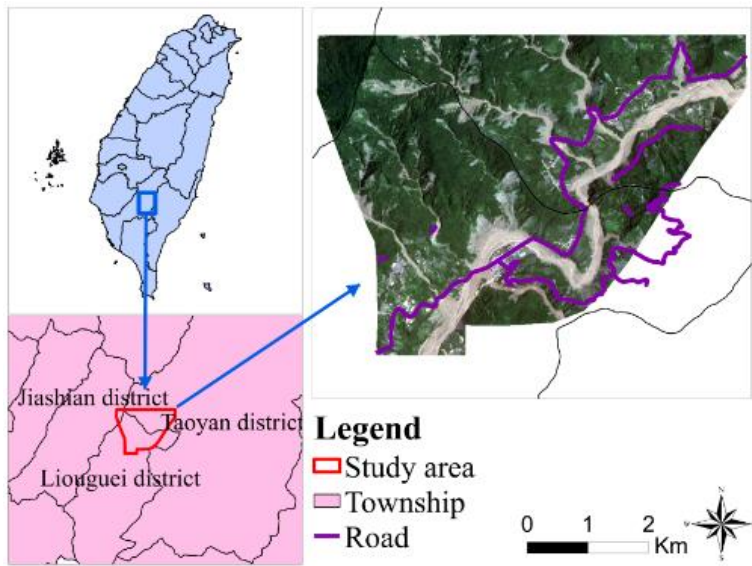
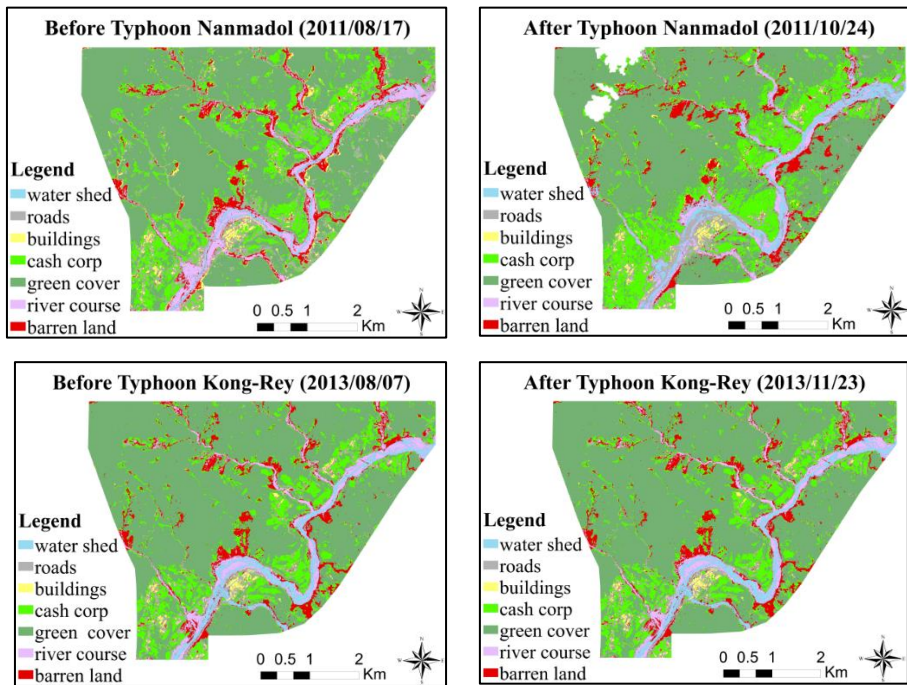
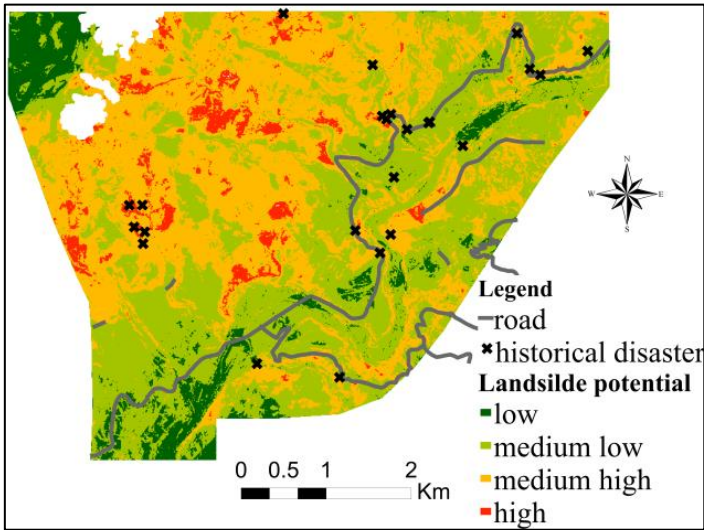


Figure 2: Study Area in the southern Taiwan, blue line depict the distribution of mountain roads.

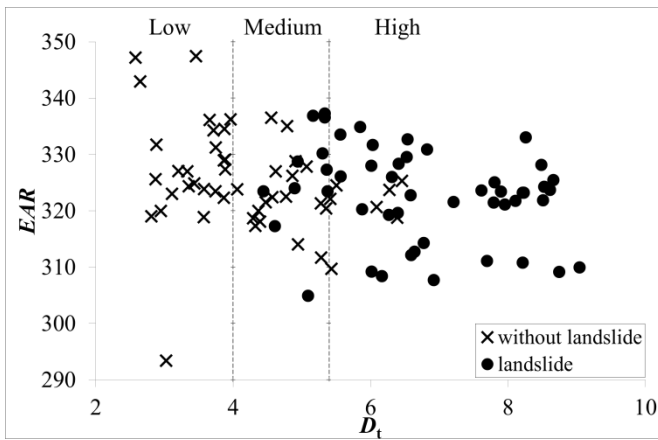


**Figure 3: Interpretation and Classification Results of Satellite Images Before (Left) and After (Right) Typhoon Nanmadol (Top) and Typhoon Kong-rey (Bottom)**

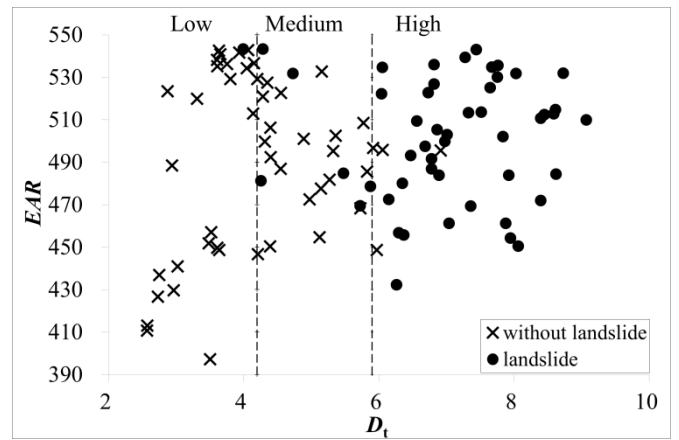


**Figure 4: Landslide Susceptibility in Study Area, in which cross symbols represent the historical disasters collected from NCDR (2017)**

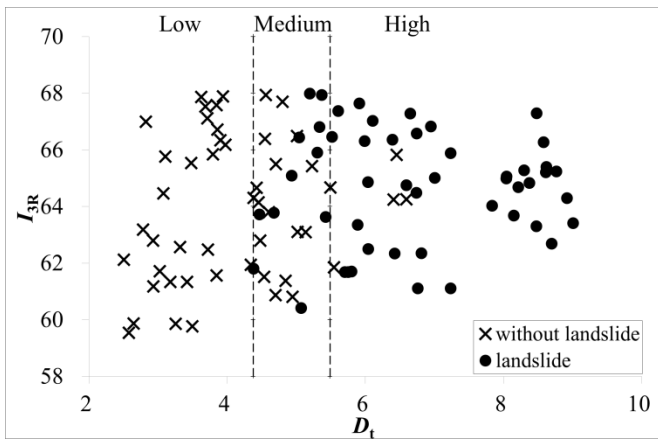
5



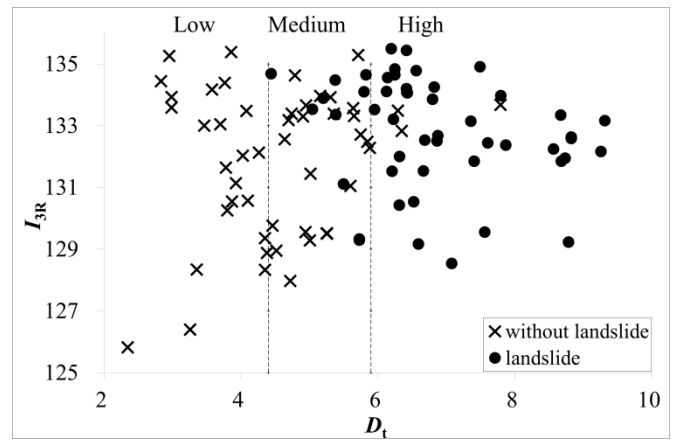
(a) Typhoon Nanmadol (2011) based on  $EAR$



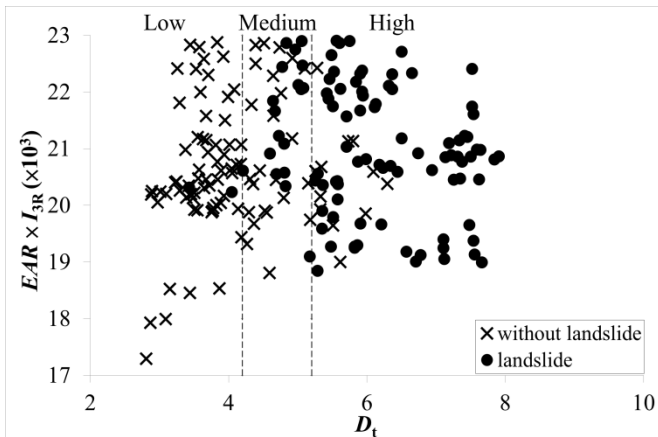
(b) Typhoon Kong-rey (2013) based on  $EAR$



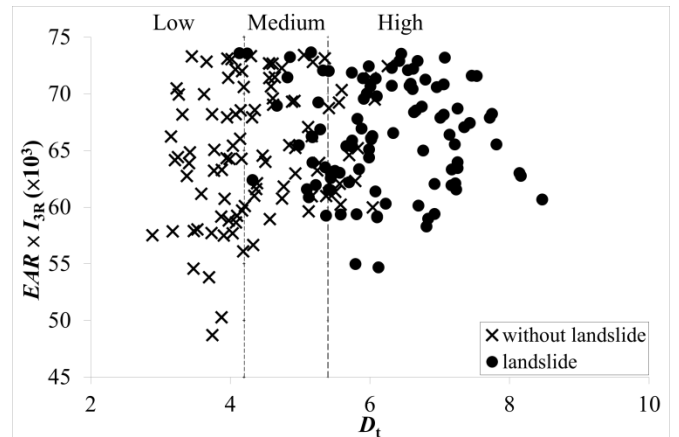
(c) Typhoon Nanmadol (2011) based on  $I_{3R}$



(d) Typhoon Kong-rey (2013) based on  $I_{3R}$

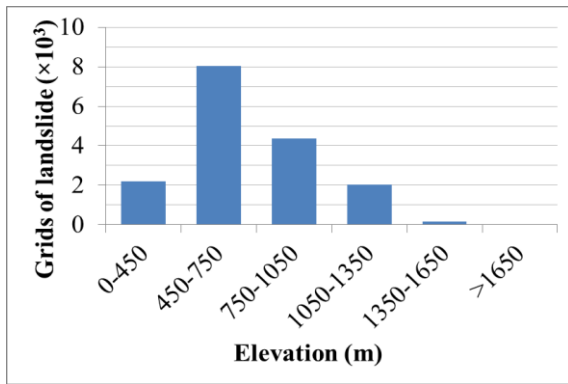


(e) Typhoon Nanmadol (2011) based on  $EAR \times I_{3R}$

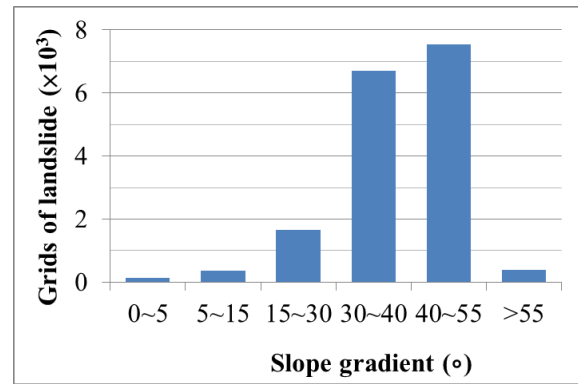


(f) Typhoon Kong-rey (2013) based on  $EAR \times I_{3R}$

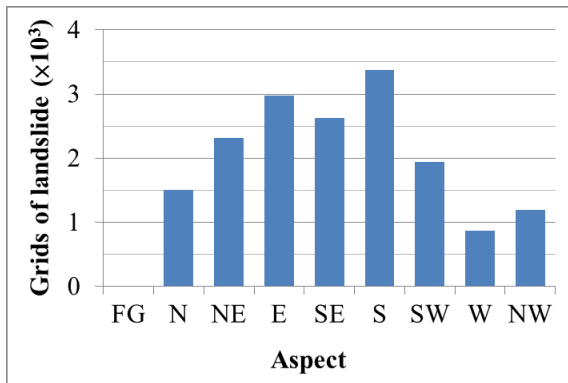
**Figure 5: Relationships among Instability Index, Effective Accumulated Rainfall, and Landslide Occurrence in Study Area after Typhoons Nanmadol (2011) and Kong-rey (2013), respectively.**



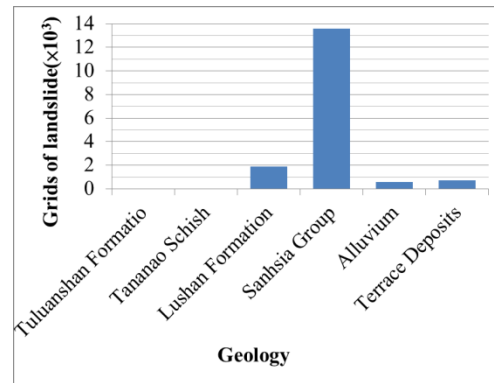
(a) Elevation



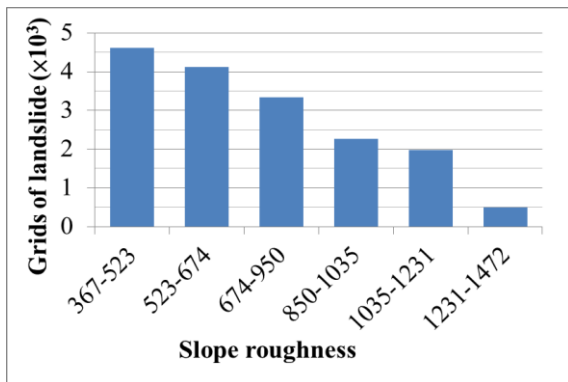
(b) Slope gradient



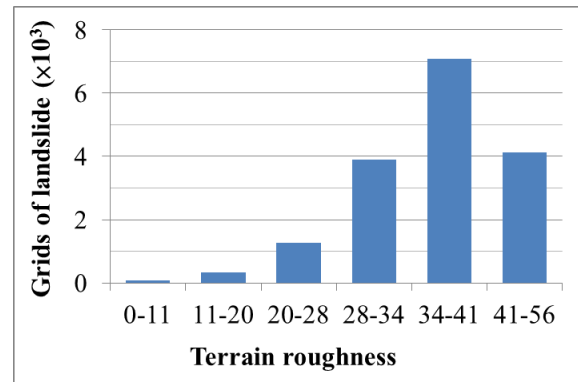
(c) Aspect



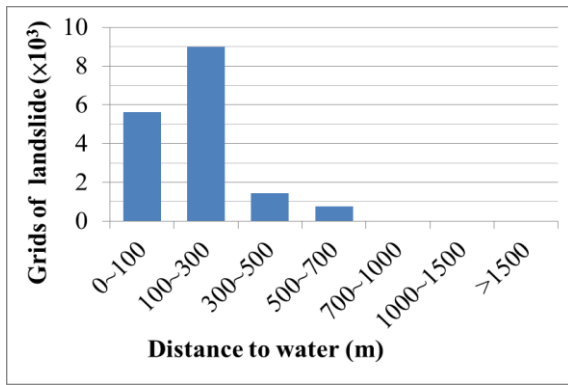
(d) Geology



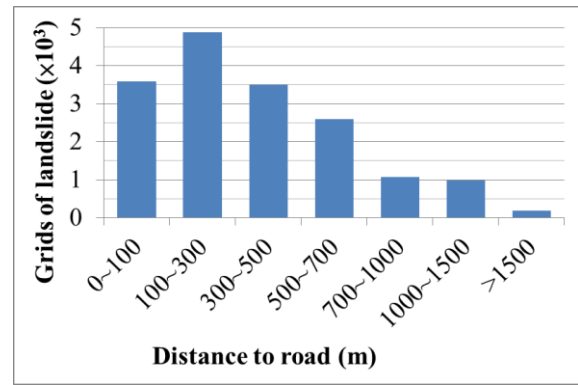
(e) Slope roughness



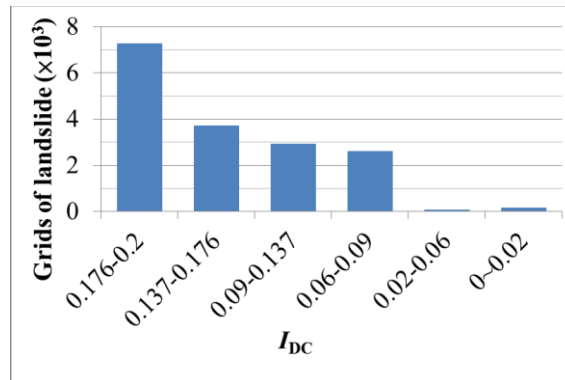
(f) Terrain roughness



(g) Distance to water



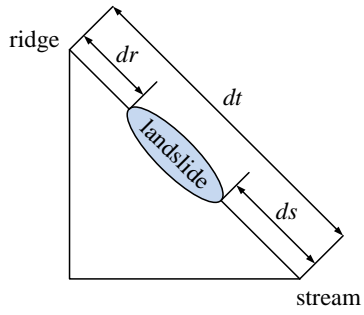
(h) Distance to road



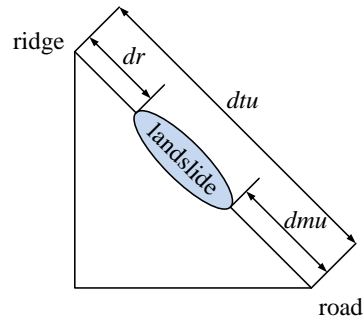
(i) Degree of land disturbance

**Figure 6: Relationships between Landslide Predisposing Factors and Number of Landslide Pixels in Study Area**

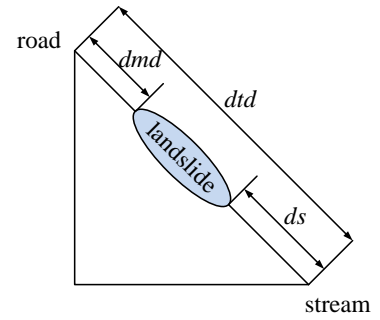
5



(a) Entire slope



(b) Slope above mountain road

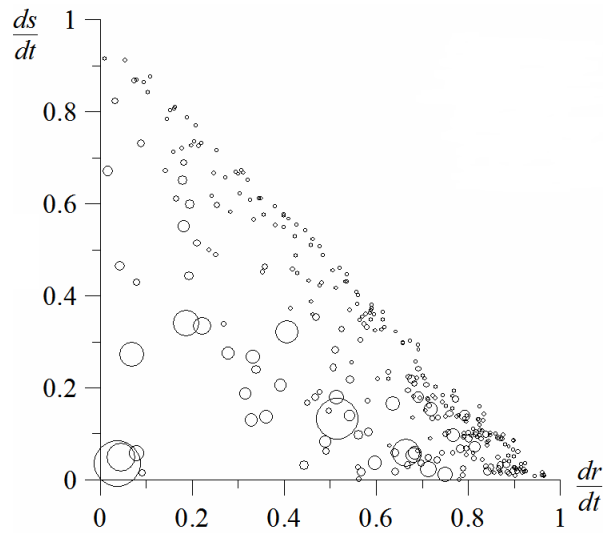


(c) Slope below mountain road

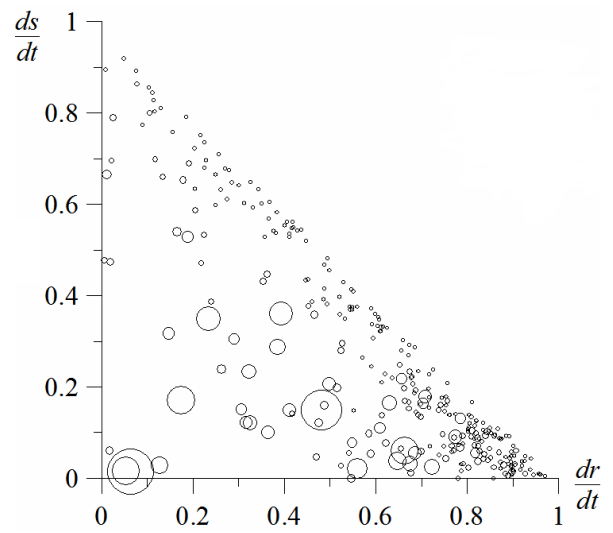
**Figure 7: Diagrams of Landslide Area on Slope, in which  $dr$  represents the distance between the highest point of a landslide area and the nearest ridge,  $ds$  the distance between the lowest point of the landslide area and the nearest stream, and  $dt$  the distance between ridge and stream.**

10

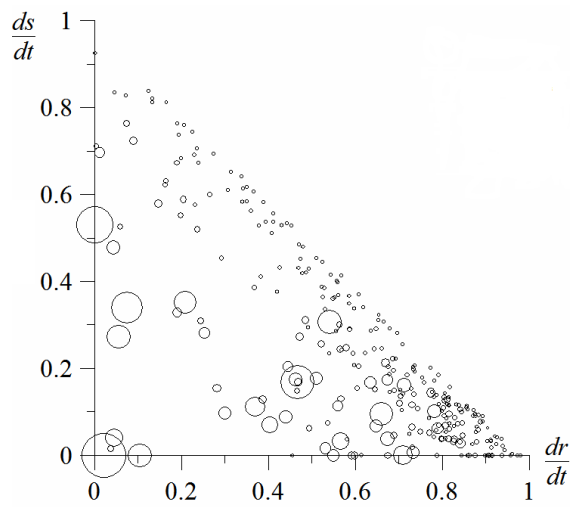




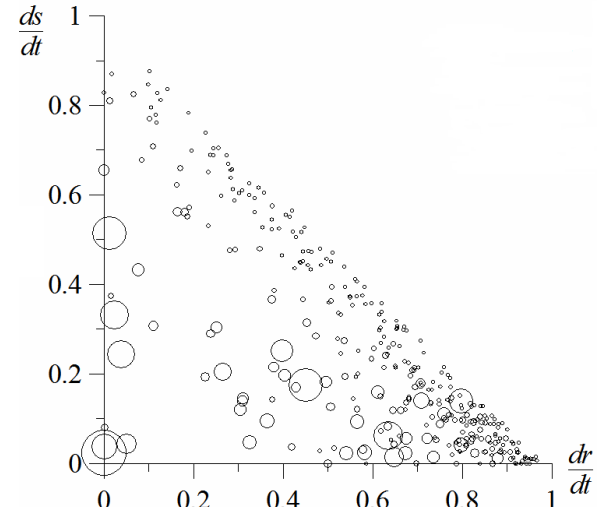
(a) Before Typhoon Nanmadol in 2011



(b) After Typhoon Nanmadol in 2011



(c) Before Typhoon Kong-rey in 2013



(d) After Typhoon Kong-rey in 2013

○ 0.05 km<sup>2</sup> ○ 0.03 km<sup>2</sup> ○ 0.01 km<sup>2</sup> ○ 0.005 km<sup>2</sup> ○ 0.001 km<sup>2</sup>

**Figure 8: Spatial Distribution of Bare Land in the Study Area before and after the Typhoons Nanmadol (Top) and Typhoon Kong-rey (Bottom), the scales of bubble reflect the area of each bare land.**

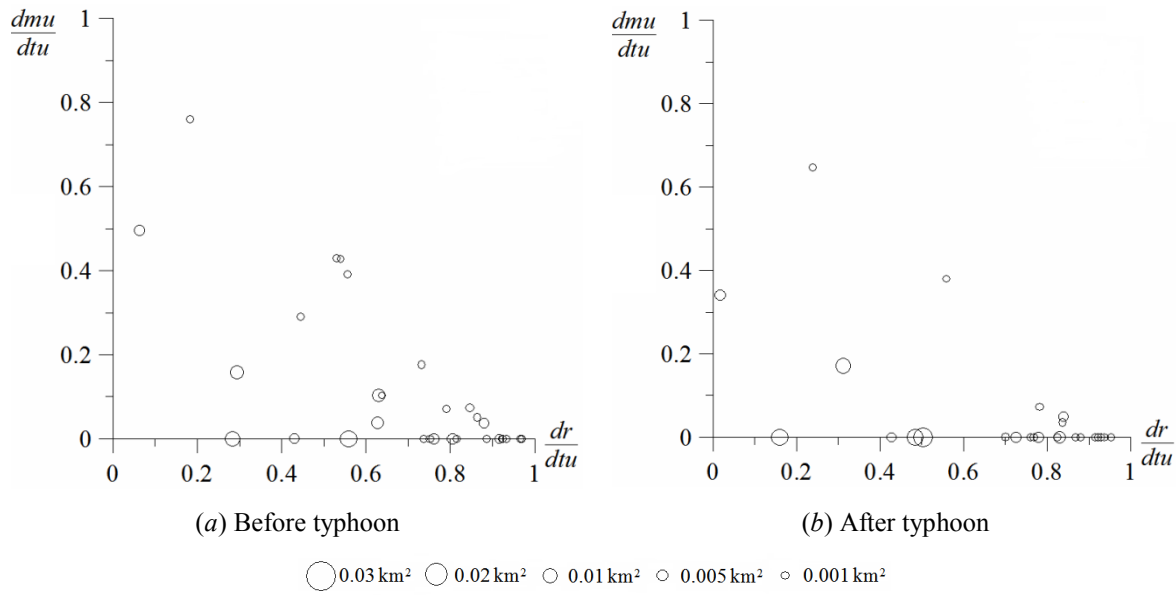


**Figure: 9 Spatial Distribution of Bare Land on Slopes above Mountain Roads in the Study Area before and after Typhoon Kongrey in 2013, the scales of bubble reflect the area of each bare land.**

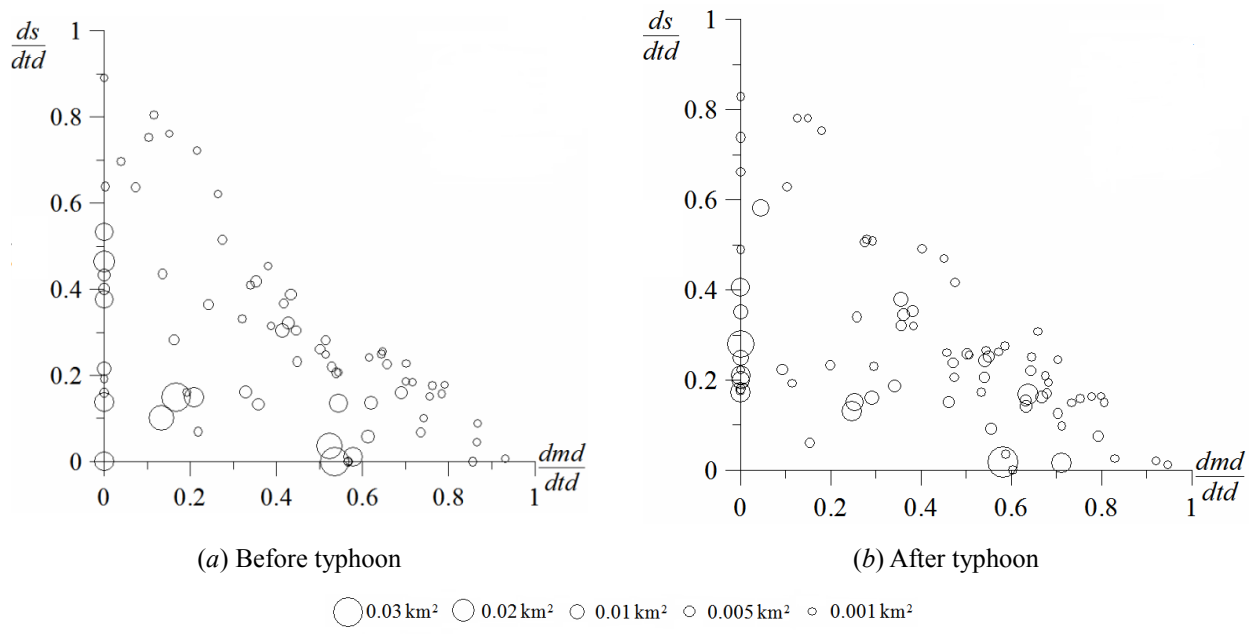


**Figure 10: Spatial Distribution of Bare Land on Slopes below Mountain Roads in the Study Area before and after Typhoon Kongrey in 2013, the scales of bubble reflect the area of each bare land.**

**Table 1: Relationship Table of Error Matrix (Verbyla, 1995)**

		Actual ground surface		Total
		Class A	Class B	
Classification results	Class A	$X_{11}$	$X_{12}$	$X_{+i}$
	Class B	$X_{21}$	$X_{22}$	$X_{+i}$
Total		$X_{i+}$	$X_{i+}$	$X_{++}$

**Table 2: Error Matrix of Interpretation Results of Satellite Images before and after Typhoon Kong-rey in 2013**

	Water	Roads	Buildings	Crops	Vegetation	River channels	Bare land	Subtotal	User's accuracy (%)
Water	15	0	0	0	0	0	0	15	100
Roads	1	7	2	0	0	3	0	10	70
Buildings	2	0	22	0	0	0	0	24	92
Crops	0	4	0	11	0	0	1	16	69
Vegetation	1	5	0	12	25	0	2	45	56
River channels	6	3	1	0	0	24	4	38	63
Bare land	0	6	0	2	0	1	18	27	67
Subtotal	25	25	25	25	25	25	25	175	
Producer's accuracy (%)	60	28	88	44	100	95	72		
<i>Kappa = 0.64; OA = 70%</i>									

**Table 3: Interpretation Results of Satellite Images before and after Typhoons Nanmadol and Kong-rey**

Time of satellite image	<i>Kappa</i>	<i>OA (%)</i>
Before Typhoon Nanmadol (2011.08.17)	0.64	69
After Typhoon Nanmadol (2012.10.14)	0.53	61
Before Typhoon Kong-rey (2013.08.17)	0.66	71
After Typhoon Kong-rey (2013.11.23)	0.64	70

**Table 4: Scores of Index for Disturbance Condition (revised from Chen et al., 2009, 2013)**

Index for disturbance condition	Bare land	Roads	Buildings	Crops	Vegetation
Score	5	4	3	2	1

**Table 5: Information of Weather Stations Used in This Study (Central Weather Bureau)**

Station No.	Station name	Longitude (degrees)	Latitude (degrees)	X(TWD97 Taiwan)	Y(TWD97 Taiwan)
C1O880	Guan-shan	120.5941	23.1734	208443.362	2563542.352
C0V150	Biao-hu	120.6647	23.2602	215693.732	2573135.951
C1V220	Hsiao Guan-shan	120.8136	23.1542	230913.463	2561372.400
C1V230	Gao-jhong	120.7167	23.1349	220987.130	2559250.525
C1V240	Sin-fa	120.6601	23.0521	215169.331	2550097.989
C0V250	Jia-sian	120.5918	23.0801	208178.971	2553211.279
C1V270	Xi-nan	120.8064	23.0760	230166.772	2552711.336



**Table 6: Effective Accumulated Rainfall and Intensity of Rolling Rainfall Observed at Weather Stations during Typhoon Nanmadol and Typhoon Kong-rey**

Weather station name	2011 Typhoon Nanmadol		2013 Typhoon Kong-rey	
	<i>EAR</i>	Max $I_{3R}$	<i>EAR</i>	Max $I_{3R}$
Guan-shan	73.79	57	376.39	146.5
Biao-hu	68.19	38.5	412.97	145
Hsiao Guan-shan	100.82	47.5	414.91	122.5
Gaojhong	336.97	68.5	543.85	135.5
Sinfa	503.94	61	288.35	122.5
Jiasian	378.92	45.5	233.12	100.5
Xi-nan	191.95	48	518.48	101.5

5

**Table 7: Correlation Test Results Between the Predisposing Factors**

	Elevation	Slope gradient	Aspect	Slope roughness	Terrain roughness	Distance to water	Distance to road	$I_{DC}$	$EAR$
Elevation	1	0.39	-0.01	0.47	0.99	0.52	0.62	-0.23	-0.66
Slope gradient	-	1	-0.07	0.85	0.37	0.11	0.18	-0.09	-0.19
Aspect	-	-	1	-0.09	-0.03	0.13	0	0	-0.12
Slope roughness	-	-	-	1	0.48	0.14	0.23	-0.11	-0.25
Terrain roughness	-	-	-	-	1	0.53	0.63	-0.24	-0.67
Distance to water	-	-	-	-	-	1	0.49	-0.21	-0.47
Distance to road	-	-	-	-	-	-	1	-0.14	-0.61
$I_{DC}$	-	-	-	-	-	-	-	1	0.14
$EAR$	-	-	-	-	-	-	-	-	1

**Table 8: Paired Sample t Test Results Between Elevation and Terrain Roughness and Slope Gradient and Slope Roughness**

	Paired difference					t	Degree of freedom	Significance (Two-tailed)
	Mean	S.D.	Standard error of mean	95% confidence interval of difference				
				Upper limit	Lower limit			
Elevation-terrain roughness	-2.69	46.5	0.07	-2.83	-2.54	-36.8	407493	0
Slope gradient-slope roughness	-0.11	7.9	0.01	-0.14	-0.08	-9.1	407493	0

**Table 9: Weights and Scores of Predisposing Factors after Rainfall Brought by Typhoon Nanmadol in 2011**

Predisposing factor	Class No.	Number of pixel	Number of landslides	Landslide percentage	Score	Predisposing factor	Class No.	Number of pixel	Number of landslides	Landslide percentage	Score
Elevation ( $E_l$ )	1	0	0	0	1	Slope gradient ( $S_s$ )	1	0	0	0	1
	2	0	0	0	1		2	4096	378	0.092	9.21
	3	8377	175	0.021	4.62		3	74623	7545	0.101	10
	4	45633	2043	0.045	8.75		4	119696	6704	0.056	5.99
	5	84049	4370	0.052	10		5	100477	1666	0.017	2.48
	6	209648	8023	0.038	7.62		6	61442	369	0.006	1.53
	7	59787	2182	0.036	7.32		7	47160	131	0.003	1.25
$\sigma=0.021, V=0.764, W=0.087$						$\sigma=0.044, V=1.111, W=0.127$					
Aspect ( $A_s$ )	1	72961	3381	0.046	10	$I_{DC}$	1	18462	7278	0.394	10
	2	129113	4569	0.035	7.87		2	37591	3735	0.099	3.26
	3	95534	3839	0.040	8.80		3	33686	2924	0.087	2.97
	4	75666	3505	0.046	10		4	78519	2611	0.033	1.75
	5	34220	1499	0.044	9.51		5	216535	83	0	1
	6	0	0	0	1		6	22701	162	0.007	1.15
$\sigma=0.018, V=0.504, W=0.058$						$\sigma=0.148, V=1.431, W=0.163$					
Slope roughness ( $S_r$ )	1	32672	4136	0.127	10	Terrain roughness ( $T_r$ )	1	20809	496	0.024	1
	2	83465	7085	0.084	7.01		2	36844	1969	0.053	10
	3	104560	3903	0.037	3.6		3	47547	2257	0.047	8.18
	4	75349	1260	0.017	2.12		4	67105	3330	0.050	8.84
	5	51143	342	0.007	1.4		5	98836	4121	0.042	6.43
	6	60305	67	0.001	1		6	136353	4620	0.034	4.05
$\sigma=0.05, V=1.098, W=0.125$						$\sigma=0.011, V=0.266, W=0.03$					
Distance to water ( $D_s$ )	1	134641	5610	0.042	8.08	Distance to road ( $D_r$ )	1	165766	3581	0.022	1
	2	169659	8983	0.053	10		2	120008	4871	0.041	3.08
	3	69076	1446	0.021	4.56		3	44993	3505	0.078	7.16
	4	19906	754	0.038	7.44		4	25015	2597	0.104	10
	5	8336	0	0	1		5	25101	1065	0.042	3.28
	6	5627	0	0	1		6	21848	986	0.045	3.58
	7	249	0	0	1		7	4763	188	0.039	2.96
$\sigma=0.023, V=1.029, W=0.117$						$\sigma=0.028, V=0.528, W=0.058$					

Predisposing factor	Class No.	Number of pixel	Number of landslides	Landslide percentage	Score	Predisposing factor	Class No.	Number of pixel	Number of landslides	Landslide percentage	Score
<i>EAR</i>	1	15768	139	0.00882	2.05196	Geology ( $G_s$ )	1	70071	738	0.011	2.56
	2	113386	3590	0.03166	4.77831		2	43675	598	0.014	3.02
	3	163395	7879	0.04822	6.75433		3	222814	13575	0.061	10
	4	73522	3191	0.0434	6.17931		4	70934	1882	0.027	4.92
	5	26439	1994	0.07542	10		5	0	0	0	1
	6	14984	0	0	1		6	0	0	0	1
$\sigma=0.028, V=0.797, W=0.091$						$\sigma=0.023, V=1.233, W=0.141$					

**Table 10: Intervals of Instability Index and Landslide Probability of Rainfall Factors**

Rainfall factor	$D_{t,min}$	$D_{t,max}$	$P(F)_{min}$	$P(F)_{max}$
$EAR$	2.05	9.59	0.312	0.982
$I_{3R}$	2.02	9.96	0.305	0.998

**Table 11: Accuracy of Landslide Susceptibility Map in Considering Different Rainfall Factors and Typhoons**

Typhoon event	Rainfall factor	Landslide susceptibility at locations of 24 historical disasters				Accuracy (%)	Mean accuracy (%)
		Low susceptibility	Medium low susceptibility	Medium high susceptibility	High susceptibility		
Typhoon Nanmadol (2011)	<i>EAR</i>	2	5	11	6	71%	71%
	<i>I<sub>3R</sub></i>	3	4	13	4	71%	
Typhoon Kong-rey (2013)	<i>EAR</i>	2	4	13	5	75%	75%
	<i>I<sub>3R</sub></i>	2	4	11	7	75%	

**Table 12: Numbers of Landslide Pixels in Study are corresponding to Different  $D_t$  Levels under Different Rainfall Factors after Typhoons**

Rainfall event	Numbers of landslide and non-landslide pixel (Proportion of landslide pixel)			Number of pixels in each level based on $EAR$			Number of pixels in each level based on $I_{3R}$		
				$D_t$ level			$D_t$ level		
	Low	Medium	High	Low	Medium	High			
Typhoon Nanmadol (2011)	Whole area	Landslide	16793	211	3031	13551	216	3603	12974
		Non-landslide	390710	168259	166289	56153	177396	166358	46947
		(Landslide/ Non-landslide)		0.00125	0.01822	0.24132	0.00122	0.02166	0.27635
	Random sampling	Landslide	50	0	11	39	0	12	38
		Non-landslide	50	24	21	5	25	21	4
Typhoon Kong-rey (2013)	Whole area	Landslide	20771	392	4303	16076	434	4482	15855
		Non-landslide	396175	182810	181824	31541	181079	185305	29791
		(Landslide/ Non-landslide)		0.00214	0.02367	0.50969	0.00240	0.02419	0.53221
	Random sampling	Landslide	50	1	6	43	0	11	39
		Non-landslide	50	27	20	3	20	27	3